Direct Space Decomposition of ELI-D: Interplay of Charge Density and Pair-Volume Function for Different Bonding Situations

Frank R. Wagner,* Miroslav Kohout, and Yuri Grin

Max-Planck-Institut für Chemische Physik fester Stoffe, Nöthnitzer Straβe 40, 01187 Dresden, Germany

Received: March 14, 2008; Revised Manuscript Received: June 25, 2008

The topological features, i.e., gradients and curvatures of the same-spin electron pair restricted electron localizability indicator (ELI-D) in position space are analyzed in terms of those of the electron density and the pair-volume function. The analysis of the topology of these constituent functions and their interplay on ELI-D attractor formation for a number of molecules representing chemically different bonding situations allows distinguishing between different chemical bonding scenarios on a quantum mechanical basis without the recourse to orbitals. The occurrence of the Laplacian of the electron density in the expression for the Laplacian of ELI-D allows us to establish a physical link between electron localizability and electron pairing as displayed by ELI-D and the role of Laplacian of the density in this context.

1. Introduction

The topology of the charge density in chemical systems has been analyzed for more than 30 years.[1] A quantum mechanically profound way to do this has been developed by Bader and co-workers, who established the "quantum theory of atoms-in-molecules" (QTAIM) method.[2] The Laplacian of the charge density plays a central role in this approach, where it occurs as a nonclassical kinetic energy density in the local form of the virial theorem. Additionally, a connection between the Laplacian of the charge density and the spatial localization of the Fermi hole has been postulated from observations that the Fermi hole is most localized when the position of the reference electron coincides with a local minimum of the Laplacian of the charge density in the valence shell of an atom.[3] A nonempirical measure of electron localizability has been developed in the framework of electron localizability indicators based on the electronic pair density, where the functional ELI has been derived within the restricted populations approach.[4] In the variant called ELI-D, which is based on D-restricted (i.e., pair-restricted) space partitioning, the electron localizability information is produced from the simple product form of the one-electron property charge density with the two-electron property pair-volume function.[5,6] ELI-D is always positive and its values are a direct measure of electron localizability based on event probabilities.[7] The appealing simple product form of ELI-D has been utilized to exactly decompose it into additive partial ELI-D distributions from, e.g., orbital densities.[6] In the present contribution, the orbital point of view will be completely omitted. Instead, the interplay between the topologies of the charge density and the pair-volume function in view of the formation of specific ELI-D topologies for different chemical bonding scenarios will be analyzed.

2. Theory

ELI-D has been defined to monitor the amount of σ-spin electrons necessary to locally build a fixed fraction of a σ-spin electron pair,[5,6] which is given in the continuous representation as

$$\Upsilon_D^{\sigma}(\mathbf{r}) = \rho_{\sigma}(\mathbf{r}) \cdot \tilde{V}_D(\mathbf{r}) = \rho_{\sigma}(\mathbf{r}) \cdot \left(\frac{12}{g(\mathbf{r})}\right)^{3/8} \tag{1}$$

where the Fermi hole curvature $g(\mathbf{r})$ for time-independent single-determinantal wave function from orbitals φ reads

$$g(\mathbf{r}) = \sum_{i<j}^{\mathrm{occ},\sigma} |\varphi_i(\mathbf{r})\nabla\varphi_j(\mathbf{r}) - \varphi_j(\mathbf{r})\nabla\varphi_i(\mathbf{r})|^2$$
$$= \rho_{\sigma}(\mathbf{r})\left(\sum_{i}^{\mathrm{occ},\sigma} |\nabla\varphi_i(\mathbf{r})|^2 - \frac{1}{4}\frac{(\nabla\rho_{\sigma}(\mathbf{r}))^2}{\rho_{\sigma}(\mathbf{r})}\right) \tag{2}$$

Thus, the ELI-D distribution in position space can be represented as a product of two scalar fields in position space (eq 1), the well-known σ-spin electron density $\rho_{\sigma}(\mathbf{r})$ being a one-particle property, and the so-called pair-volume function $\tilde{V}_D(\mathbf{r})$ being a two-particle property because it is proportional to the volume needed to locally encompass a fixed fraction of a same-spin electron pair of σ-spin electrons.[6] In the following the spin index will be always skipped for brevity. The respective generic shapes are exemplarily given in Figure 1 for an isolated Ar atom. It can be seen that the electron density and the pair-volume function display a mutually reciprocal behavior. This is expected from the general behavior of the Fermi-hole curvature, which is given for the homogeneous electron gas in the framework of Hartree−Fock theory[8] by the following proportionality

$$g(\mathbf{r}) \propto \rho(\mathbf{r})^{8/3} \tag{3}$$

Therefore (eqs 1 and 3), as a zeroth-order estimate for the behavior of the pair-volume function in a molecular system, it is expected to behave like the inverse of the electron density.

$$\tilde{V}_D(\mathbf{r}) \propto g(\mathbf{r})^{-3/8} \sim \rho(\mathbf{r})^{-1} \tag{4}$$

Accordingly, the gradient of the pair-volume function is expected to typically behave according to

$$\frac{\partial}{\partial x}\tilde{V}_D(\mathbf{r}) \sim -\frac{1}{(\rho(\mathbf{r}))^2}\frac{\partial}{\partial x}\rho(\mathbf{r}) \tag{5}$$

i.e., the gradients of $\rho(\mathbf{r})$ and $\tilde{V}_D(\mathbf{r})$ are expected to display opposite sign. Combining eqs 1 and 4 it is obvious that the rich ELI-D topology arises from the locally varying deviations of

* Corresponding author. E-mail: wagner@cpfs.mpg.de.

10.1021/jp8022315 CCC: $40.75
Published on Web 09/17/2008

the pair-volume function from the zeroth-order behavior. To better understand the physical mechanism of ELI-D attractor formation, it is necessary to investigate the cooperative action of the electron density and the pair-volume function.

The generic topology of the electron density in a chemical system has been described in detail by Bader.[2] Since the electron density for an isolated atom is known to decay in a piecewise exponential way,[9] for molecules or solids local maxima (attractors) of $\rho(\mathbf{r})$ are expected only at the core positions, which is indeed the case for the majority of chemical systems. Noteworthy, however, a number of exceptions are known to exist, where non-nuclear maxima are observed.[10] The number and type of critical points ($n(3,-3)$, $n(3,-1)$,...), which can simultaneously occur in a molecular system is covered by the Poincaré−Hopf theorem, which yields for molecules in the case of the electron density[11]

$$n(3,-3)-n(3,-1)+n(3,+1)-n(3,+3)=1 \quad (6)$$

For the pair-volume function tending to infinity at infinite distance from the nucleus, a complementary sum rule is valid for molecules

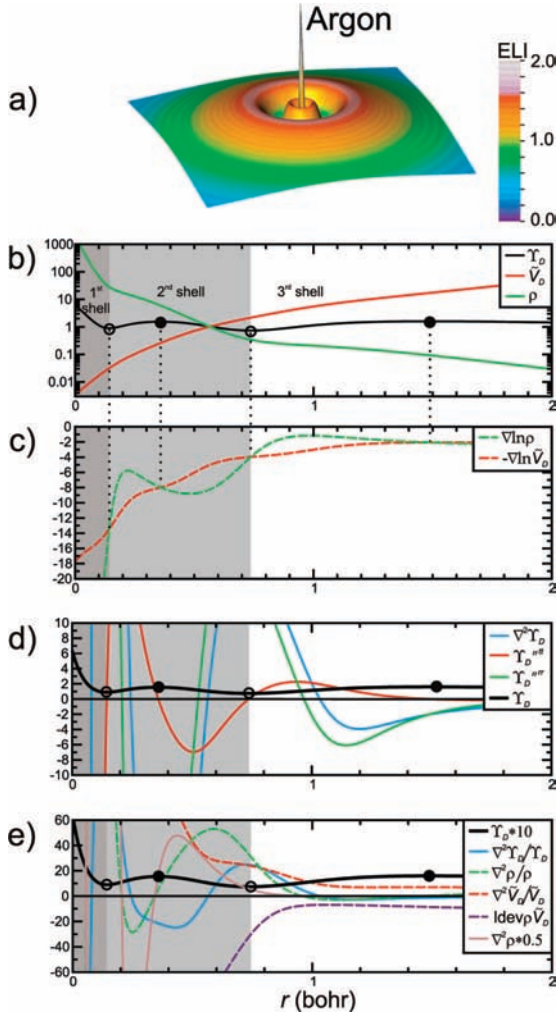

Figure 1. Argon atom: (a) ELI-D in combined height field/color map representation; various quantities along radial line starting from nucleus ($r = 0$). Critical points are indicated with black filled spheres (attractors) and hollow circles. (b) Behavior (log scale) of ELI-D, $\tilde{V}_D$ and ρ. (c) Behavior of $\nabla \ln \rho$ and $-\nabla \ln \tilde{V}_D$, ELI-D critical point formation (eq 10). (d) Laplacian of ELI-D, radial ($\Upsilon_D''^{rr}$) and transverse ($\Upsilon_D''^{tt}$) ELI-D curvatures. (e) Decomposition of relative ELI-D Laplacian (eq 22), $\mathrm{ldev}\rho\tilde{V}_D = 2\nabla \ln \rho \cdot \nabla \ln \tilde{V}_D$.

$$n(3,-3)-n(3,-1)+n(3,+1)-n(3,+3)=-1 \quad (7)$$

whereas for crystals the Euler characteristic equals 0 for both quantities.

It is instructive to relate the topology of ELI-D with the topology of its constituents. The gradient of ELI-D, cf. eq 1, is given according to

$$\nabla \Upsilon_D^\sigma = \nabla\rho \cdot \tilde{V}_D + \rho \cdot \nabla \tilde{V}_D \quad (8)$$

At an ELI-D critical point $\mathbf{r}_c$ its gradient vanishes by definition (eq 9). For $\nu = x, y, z$

$$\frac{\partial \Upsilon_D^\sigma}{\partial \nu} = \frac{\partial \rho}{\partial \nu}\cdot \tilde{V}_D + \rho \cdot \frac{\partial \tilde{V}_D}{\partial \nu} = 0 \qquad \text{at } \mathbf{r}_c \text{ of } \Upsilon_D^\sigma \quad (9)$$

In this case the following relations (eqs 10a,b) (using convention $\partial\rho/\partial\nu = \rho'^\nu$) are always fulfilled.

$$\frac{\rho'^\nu}{\rho} = -\frac{\tilde{V}_D'^\nu}{\tilde{V}_D} \qquad \text{at } \mathbf{r}_c \text{ of } \Upsilon_D^\sigma \quad (10a)$$

or, equivalently,

$$(\ln \rho)'^\nu = -(\ln \tilde{V}_D)'^\nu \qquad \text{at } \mathbf{r}_c \text{ of } \Upsilon_D^\sigma \quad (10b)$$

Therefore, either a critical point of ELI-D is simultaneously a critical point of both constituents, $\rho(\mathbf{r})$ and $\tilde{V}_D(\mathbf{r})$ or they both have equal logarithmic derivative magnitudes but in opposite directions. Because the logarithmic derivatives of the density and the pair-volume function play an important role in ELI-D critical point formation, it should be noticed that eqs 10a,b can be seen as the special case for the generally valid expression of the logarithmic derivative of ELI-D obtained from eq 8 via division by the local ELI-D value.

$$\frac{\Upsilon_D^{\sigma\prime\nu}}{\Upsilon_D^\sigma} = \frac{\rho'^\nu}{\rho} + \frac{\tilde{V}_D'^\nu}{\tilde{V}_D} \quad (11a)$$

or, equivalently,

$$(\ln \Upsilon_D^\sigma)'^\nu = (\ln \rho)'^\nu + (\ln \tilde{V}_D)'^\nu \quad (11b)$$

The type of the ELI-D critical point as defined by its rank and signature is determined from the eigenvalues of the corresponding Hessian matrix, i.e., the curvatures of ELI-D. The rank is the number of nonzero Hessian eigenvalues and the signature is given as the number of positive minus the number of negative Hessian eigenvalues.

The elements of the Hessian matrix of ELI-D at the critical point $\mathbf{r}_c$ are given as

$$\Upsilon_D^{\sigma\prime\prime\mu\nu} = \rho''^{\mu\nu}\tilde{V}_D + \rho''^{\mu}\tilde{V}_D'^{\nu} + \rho'^{\nu}\tilde{V}_D'^{\mu} + \rho\tilde{V}_D''^{\mu\nu} \quad (12)$$

Diagonalizing the Hessian of ELI-D eq 12 requires matrix elements to obey

for $\kappa \neq \lambda$:

$$\Upsilon_D^{\sigma\prime\prime\kappa\lambda} = \rho''^{\kappa\lambda}\tilde{V}_D + \rho\tilde{V}_D''^{\kappa\lambda} + \rho''^{\kappa}\tilde{V}_D'^{\lambda} + \rho'^{\lambda}\tilde{V}_D'^{\kappa} = 0$$

for $\kappa = \lambda$:

$$\Upsilon_D^{\sigma\prime\prime\kappa\kappa} = \rho''^{\kappa\kappa}\tilde{V}_D + \rho\tilde{V}_D''^{\kappa\kappa} + 2\rho''^{\kappa}\tilde{V}_D'^{\kappa} \quad (13)$$

Here it is important to realize that the Hessian eigenvectors for ρ'', $\tilde{V}_D''$ and $\Upsilon_D^\sigma{}''$ separately need not necessarily be the same. Clearly, the derivatives of $\rho(\mathbf{r})$ and $\tilde{V}_D(\mathbf{r})$ have to be taken in those directions κ and λ, which are defined by the eigenvectors of the Hessian of ELI-D.

If the critical point of ELI-D is also a critical point of either $\rho(\mathbf{r})$ or $\tilde{V}_D(\mathbf{r})$, the curvatures of ELI-D simplify according to

$$Y_D^{\sigma\,\prime\prime\kappa\kappa} = \rho^{\prime\prime\kappa\kappa}\tilde{V}_D + \rho\tilde{V}_D{}^{\prime\prime\kappa\kappa}, \text{ at } \mathbf{r}_c \text{ of } Y_D^\sigma \wedge \mathbf{r}_c \text{ of } \rho \text{ or } \tilde{V}_D \tag{14}$$

The signature of the ELI-D critical point is given by the signs of the Hessian eigenvalues $Y_D^{\sigma\,\prime\prime\kappa\kappa}$(denoted $Y_D^{\sigma\,\prime\prime}$ in the following), which are each determined by the sign of the dominating term, $\rho\cdot\tilde{V}_D{}^{\prime\prime\kappa\kappa}$, $\rho^{\prime\prime\kappa\kappa}\cdot\tilde{V}_D$ or $2\rho^{\prime\kappa}\,\tilde{V}_D{}^{\prime\kappa}$ (eq 13), respectively. Again, an alternative formulation is obtained dividing the Hessian eigenvalues by the local ELI-D value (eq 15). This transformation keeps the sign of each of the three terms at any point in space such that, e.g., a region of negative $\rho^{\prime\prime\kappa\kappa}\cdot\tilde{V}_D$ is identical to the one for negative $\rho^{\prime\prime\kappa\kappa}/\rho$. Hence, it is to be interpreted as a type of rescaling of the individual terms, which serves to separate the density from the pair-volume curvature term and vice versa.

$$\frac{Y_D^{\sigma\,\prime\prime\kappa\kappa}}{Y_D^\sigma} = \frac{\tilde{V}_D{}^{\prime\prime\kappa\kappa}}{\tilde{V}_D} + \frac{\rho^{\prime\prime\kappa\kappa}}{\rho} + 2\frac{\rho^{\prime\kappa}}{\rho}\frac{\tilde{V}_D{}^{\prime\kappa}}{\tilde{V}_D} \tag{15}$$

Although eq 15 is valid for any point in space, eq 16 is obtained at an ELI-D critical point utilizing eq 10.

$$\frac{Y_D^{\sigma\,\prime\prime\kappa\kappa}}{Y_D^\sigma} = \frac{\tilde{V}_D{}^{\prime\prime\kappa\kappa}}{\tilde{V}_D} + \frac{\rho^{\prime\prime\kappa\kappa}}{\rho} - 2\left(\frac{\rho^{\prime\kappa}}{\rho}\right)^2, \text{ at a critical point of } Y_D^\sigma \tag{16}$$

The gradient term $2\rho'\,\tilde{V}_D{}'$ occurring in eq 15 is never positive at an ELI-D critical point:

$$2\rho^{\prime\kappa}\cdot\tilde{V}_D{}^{\prime\kappa} \le 0, \text{ at } \mathbf{r}_c \text{ of } Y_D^\sigma \tag{17}$$

Because both $\rho(\mathbf{r})$ and $\tilde{V}_D(\mathbf{r})$ have positive values, the signs of $\rho\cdot\tilde{V}_D{}^{\prime\prime\kappa\kappa}$ and $\rho^{\prime\prime\kappa\kappa}\cdot\tilde{V}_D$ values or, equivalently, $\tilde{V}_D{}^{\prime\prime\kappa\kappa}/\tilde{V}_D$ and $\rho^{\prime\prime\kappa\kappa}/\rho$ values, are given by that of the respective second derivative. Utilizing the zeroth-order estimate for the pair-volume function behavior (eq 4) the curvature of $\tilde{V}_D(\mathbf{r})$ is related to $\rho(\mathbf{r})$ according to

$$\tilde{V}_D{}^{\prime\prime\kappa\kappa} \sim -\frac{1}{\rho}\left[\frac{\rho^{\prime\prime\kappa\kappa}}{\rho} - 2\left(\frac{\rho^{\prime\kappa}}{\rho}\right)^2\right] \tag{18}$$

Thus, in case of a zero density derivative the curvatures of $\tilde{V}_D(\mathbf{r})$ and $\rho(\mathbf{r})$ are expected to display opposite signs in same directions. At an ELI-D critical point eq 18 can be expressed alternatively utilizing eq 10a

$$\tilde{V}_D{}^{\prime\prime\kappa\kappa} \sim -\frac{1}{\rho}\left[\frac{\rho^{\prime\prime\kappa\kappa}}{\rho} + 2\frac{\rho^{\prime\kappa}}{\rho}\frac{\tilde{V}_D{}^{\prime\kappa}}{\tilde{V}_D}\right], \text{ at } \mathbf{r}_c \text{ of } Y_D^\sigma \tag{19}$$

In this form, the validity of this estimate can be easily checked for the examples analyzed below, because the values for the square bracket terms are given in Table 1. It will be seen that the sign of the pair-volume curvature at ELI-D critical points can be inferred according to eq 19 in most cases.

For the charge density the definition of the derived quantity $-\nabla^2\rho$ called the local charge concentration has proven useful.[12] Mathematically, it measures the deviation of the local density value from the spatially averaged value of its immediate surroundings. Physically, it represents a nonclassical contribution to the electronic kinetic energy density, which integrates to zero for the whole system. The sign of the density Laplacian signals the type of local imbalance between the potential energy density and the kinetic energy density according to the local virial theorem of Bader.[2] Recently, it has been claimed on the basis of an observed empirical homeomorphism between the Laplacian of the density and the Laplacian of the conditional same-spin pair density distributions for some molecules[3] that the former achieves "a clear representation of the pairing of electrons in real space".[13]

Because ELI-D represents another type of charge distribution, roughly the charge needed to create a fixed fraction of a same-spin electron pair, which is proven to be related to the local pairing of same spin electrons,[4] it is of interest to investigate $\nabla^2 Y_D^\sigma$ as well (note: for physical transparency we omit the arbitrary "−" sign applied in the definition of the charge concentration). The Laplacian of ELI-D at any point in space is given as the trace of the Hessian matrix, which is invariant to a unitary transformation.

$$\nabla^2 Y_D^\sigma = \sum_{\nu=x,y,z} Y_D^{\sigma\,\prime\prime\nu\nu} = \sum_\kappa Y_D^{\sigma\,\prime\prime\kappa\kappa} \tag{20}$$

which yields utilizing eq 13

$$\nabla^2 Y_D^\sigma = \tilde{V}_D\cdot\nabla^2\rho + \rho\cdot\nabla^2\tilde{V}_D + 2\,\nabla\rho\cdot\nabla\tilde{V}_D \tag{21}$$

or, equivalently, via division by the local ELI-D value

$$\frac{\nabla^2 Y_D^\sigma}{Y_D^\sigma} = \frac{\nabla^2\rho}{\rho} + \frac{\nabla^2\tilde{V}_D}{\tilde{V}_D} + 2\frac{\nabla\rho}{\rho}\cdot\frac{\nabla\tilde{V}_D}{\tilde{V}_D}$$

$$= \frac{\nabla^2\rho}{\rho} + \frac{\nabla^2\tilde{V}_D}{\tilde{V}_D} + 2\,\nabla\ln\tilde{V}_D\cdot\nabla\ln\rho \tag{22}$$

The regions of negative $\nabla^2 Y_D^\sigma$ are identical to the regions of negative $\nabla^2 Y_D^\sigma/Y_D^\sigma$ and the same is true for the regions of negative $\nabla^2\rho$ and $\nabla^2\rho/\rho$. Equations 21 and 22 establish a relation between the Laplacian of ELI-D and the Laplacian of density, and it is of interest that the Laplacian of the density now occurs either in the form of $\tilde{V}_D\cdot\nabla^2\rho$ or equivalently $\nabla^2\rho/\rho$ as one term of the (relative) Laplacian of ELI-D. For the exemplarily chosen molecules analyzed below the role of the $\nabla^2\rho/\rho$ contributions with respect to the sign of the relative ELI-D Laplacian is displayed in Table 1 and in the figures.

3. Computational Methodology

DFT calculations have been done with the ADF program package[14] using the built-in basis sets from STOs (Slater type orbitals) of the TZ2P type (triple-ζ basis set with 2 types of polarization functions) and of the ET-pVQZ type for the cages. Exchange correlation functional BLYP was used throughout, which consists of Becke's exchange[15] and Lee, Yang, Parr's[16] correlation functional. With the exception of N_2 and F_2, where the experimental structure has been utilized, molecular structures have been obtained from full geometry optimization. In each case ELI-D, electron densities and pair-volume functions, as well as their first (gradients) and second derivatives (Hessian matrix) have been analytically calculated from the corresponding wave functions using program DGrid.[17]

4. Results for the Spherical Atom Case: Argon

As a reference for the subsequent analyses of molecules, a spherically symmetric atom is treated at first. In Figure 1b the typical behavior in position space of ELI-D and its mutually reciprocal constituents, the electron density and the pair-volume function, is exemplarily shown for the argon atom. The positions of the ELI-D critical points are related

TABLE 1: Decomposition of ELI-D Curvatures and Relative Laplacian into Density and Pair-Volume Function Contributions[a]

location	values	specification[b]	ρ''/ρ	+	$\tilde{V}_D''/\tilde{V}_D$	+	$2(\rho'/\rho)(\tilde{V}_D'/\tilde{V}_D)$	=	Y_D^σ''/Y_D^σ
			(a) C_2H_6, d(C−C) = 154 pm						
at C−C bond midpoint (D_{3d}^z)	$Y_D^\sigma = 1.971$ $\rho = 0.1153$ $\tilde{V}_D = 17.10$	z (i)	+1.72		**−4.04**		0		**−2.32**
		x, y	**−1.90**		+0.71		0		**−1.19**
		type[c]	(3, −1)		(3, +1)				(3, −3)
		Laplacian	**−2.08**		**−2.62**		0		**−4.70**
			(b) Si_2H_6, d(Si−Si) = 237 pm						
at Si−Si bond midpoint (D_{3d}^z)	$Y_D^\sigma = 2.353$ $\rho = 0.04463$ $\tilde{V}_D = 52.73$	z (i)	+0.44		**−2.42**		0		**−1.98**
		x, y	**−0.99**		+0.55		0		**−0.44**
		type[c]	(3, −1)		(3, +1)				(3, −3)
		Laplacian	**−1.54**		**−1.32**		0		**−2.86**
			(c) Ge_2H_6, d(Ge−Ge) = 246 pm						
at Ge−Ge bond midpoint (D_{3d}^z)	$Y_D^\sigma = 1.560$ $\rho = 0.03953$ $\tilde{V}_D = 39.48$	z (i)	+1.07		**−4.15**		0		**−3.08**
		x, y	**−0.88**		+0.81		0		**−0.07**
		type[c]	(3, −1)		(3, +1)				(3, −3)
		Laplacian	**−0.69**		**−2.53**		0		**−3.22**
			(d) N_2, d(N−N) = 110 pm						
at N−N bond midpoint ($D_{\infty h}^z$)	$Y_D^\sigma = 1.599$ $\rho = 0.3503$ $\tilde{V}_D = 4.56$	z (i)	+1.56		**−4.84**		0		**−3.28**
		x, y	**−2.76**		+2.69		0		**−0.07**
		type[c]	(3, −1)		(3, +1)				(3, −3)
		Laplacian	**−3.96**		+0.54		0		**−3.42**
			(e) C_2H_2, d(C−C) = 121 pm						
at C−C bond midpoint ($D_{\infty h}^z$)	$Y_D^\sigma = 1.499$ $\rho = 0.2089$ $\tilde{V}_D = 7.178$	z (i)	+0.59		**−4.69**		0		**−4.10**
		x, y	−1.78		**+2.33**		0		**+0.55**
		type[c]	(3, −1)		(3, +1)				(3, +1)
		Laplacian	**−2.97**		**−0.03**		0		**−3.00**
			(f) Ne_2, d(Ne−Ne) = 141 pm						
at INL-MV ($D_{\infty h}^z$)	$Y_D^\sigma = 0.753$ $\tilde{V}_D = 6.497$ $\rho = 0.1159$	z (i)	**+16.25**		−2.78		0		**+13.47**
		x, y	**−2.57**		+2.42		0		**−0.15**
		type[c]	(3, −1)		(3, +1)				(3, −1)
		Laplacian	**+11.11**		**+2.06**		0		**+13.17**
at atom directed (3, +1) point, ($C_{\infty v}^z$)	$Y_D^\sigma = 1.532$ $\tilde{V}_D = 2.466$ $\rho = 0.6211$	z (i)	+9.63		+7.82		**−22.99**		**−5.54**
		x, y	−4.75		**+4.98**		0		**+0.23**
		type[c]	"{3, −1}"		"{3, +3}"				(3, +1)
		Laplacian	+0.13		+17.78		**−22.99**		**−5.08**
			(g) F_2, d(F−F) = 141 pm						
at INL-MV ($D_{\infty h}^z$)	$Y_D = 1.197$ $\tilde{V}_D = 8.597$ $\rho = 0.1392$	z (i)	**+6.70**		−5.41		0		**+1.29**
		x, y	**−2.44**		+1.23		0		**−1.21**
		type[c]	(3, −1)		(3, +1)				(3, −1)
		Laplacian	+1.82		**−2.95**		0		**−1.13**
at attractor position ($C_{\infty v}^z$)	$Y_D = 1.229$ $\tilde{V}_D = 6.595$ $\rho = 0.1863$	z (i)	+6.84		**−2.45**		**−6.05**		**−1.66**
		x, y	**−2.40**		+1.95		0		**−0.45**
		type[c]	"{3, −1}"		"{3, +1}"				(3, −3)
		Laplacian	+2.04		+1.45		**−6.05**		**−2.56**
			(h) BrF, d(Br−F) = 181 pm						
at INL-MV ($C_{\infty h}^z$)	$Y_D = 1.293$ $\tilde{V}_D = 11.78$ $\rho = 0.1098$	z (i)	+5.93		**−1.92**		**−4.74**		**−0.73**
		x, y	**−1.98**		+1.47		0		**−0.51**
		type[c]	"{3, −1}"		"{3, +1}"				"{3, −3}"
		Laplacian	+1.97		+1.02		**−4.74**		**−1.75**
at attractor position ($C_{\infty v}^z$)	$Y_D = 1.346$ $\tilde{V}_D = 7.173$ $\rho = 0.1876$	z (i)	+6.74		+2.51		**−10.56**		**−1.31**
		x, y	**−2.40**		+2.36		0		**−0.04**
		type[c]	"{3, −1}"		"{3, +3}"				(3, −3)
		Laplacian	+1.94		+7.23		**−10.56**		**−1.39**
			(i) LiF, d(Li−F) = 158 pm						
at INL-MV ($C_{\infty h}^z$)	$Y_D = 1.499$ $\tilde{V}_D = 9.105$ $\rho = 0.1646$	z (i)	+7.95		+3.95		**−13.41**		**−1.51**
		x, y	**−2.55**		+2.43		0		**−0.12**
		type[c]	"{3, −1}"		"{3, +3}"				"{3, −1}"
		Laplacian	+2.85		+8.81		**−13.41**		**−1.75**
at bond directed (3,+1) point ($C_{\infty h}^z$)	$Y_D = 1.533$ $\tilde{V}_D = 5.818$ $\rho = 0.2635$	z (i)	+7.56		+6.06		**−15.30**		**−1.68**
		x, y	−3.03		**+3.04**		0		**+0.01**
		type[c]	"{3, −1}"		"{3, +3}"				(3, +1)
		Laplacian	+1.50		+12.14		**−15.30**		**−1.66**
			(j) C_6H_6, d(C−C)= 140 pm						
at 0.016 bohr beyond ring edge (C_{2v}^y)	$Y_D = 1.861$ $\tilde{V}_D = 12.02$ $\rho = 0.1549$	x (i)	+1.33		**−4.14**		0		**−2.81**
		y	**−2.19**		+1.13		−0.002		**−1.06**
		z	**−1.86**		+1.63		0		**−0.23**
		type[c]	"{3, −1}"		"{3, +1}"				(3, −1)
		Laplacian	**−2.72**		**−1.38**		−0.002		**−4.10**
at ring midpoint (D_{6h}^z)	$Y_D = 0.576$ $\tilde{V}_D = 48.55$ $\rho = 0.01187$	x, y (i)	**+3.48**		−1.38		0		**+2.10**
		z	**−0.75**		+0.66		0		**−0.09**
		type[c]	(3, +1)		(3, −1)				(3, +1)
		Laplacian	**+6.21**		−2.10		0		**+4.11**
			(k) cyclo-C_3H_6, d(C−C) = 152 pm						
at 0.51 bohr beyond ring edge (C_{2v})	$Y_D = 1.805$ $\tilde{V}_D = 18.29$ $\rho = 0.09864$	x	**−1.05**		+1.06		**−0.89**		**−0.88**
		y (i)	+1.53		**−2.92**		0		**−1.39**
		z	**−1.81**		+0.77		0		**−1.04**
		type[c]	"{3, −1}"		"{3, +1}"				(3, −3)
		Laplacian	**−1.33**		**−1.09**		**−0.89**		**−3.31**

TABLE 1: Continued

location	values	specification[b]	ρ''/ρ	+	$\tilde{V}_D''/\tilde{V}_D$	+	$2(\rho'/\rho)(\tilde{V}_D'/\tilde{V}_D)$	=	$Y_D^{\sigma}''/Y_D^{\sigma}$
at ring midpoint	$Y_D = 1.210$	x, y (i)	**+1.37**		−0.43		0		**+0.94**
(D_{3h}^{z})	$\tilde{V}_D = 12.98$	z	**−1.83**		+1.35		0		**−0.48**
	$\rho = 0.09322$	type[c]	(3, +1)		(3, −1)				(3, +1)
		Laplacian	**+0.91**		**+0.49**		0		**+1.40**
		(l) C_4H_4, d(C−C)= 149 pm							
at 0.74 bohr above	$Y_D = 1.768$	[0, 1, −1] (i)	+1.18		**−2.24**		0		**−1.06**
tetrahedron edge	$\tilde{V}_D = 20.15$	[0, 1, 1]	**−1.64**		+0.69		0		**−0.95**
(C_{2v}^{x})	$\rho = 0.08776$	[1, 0, 0]	**−0.43**		+1.45		**−1.78**		**−0.76**
		type[c]	"{3, −1}"		"{3, +1}"				(3, −3)
		Laplacian	**−0.89**		**−0.10**		**−1.78**		**−2.77**
at 0.57 bohr above	$Y_D = 1.141$	2 x face (i)	**+1.22**		−0.24		0		**+0.98**
tetrahedron face	$\tilde{V}_D = 14.09$	radial	**−0.97**		+1.45		**−0.91**		**−0.43**
(C_{3v}^{xyz})	$\rho = 0.08094$	type[c]	"{3, +1}"		"{3, −1}"				(3, +1)
		Laplacian	**+1.47**		**+0.97**		−0.91		**+1.53**
at tetrahedron	$Y_D = 0.9729$	all three	**+1.07**		−0.24		0		**+0.83**
center (T_d)	$\tilde{V}_D = 11.04$	type[c]	(3, +3)		(3, −3)				(3, +3)
	$\rho = 0.08814$	Laplacian	**+3.21**		−0.72		0		**+2.49**
		(m) B_4H_4, d(B−B) = 168 pm							
at 0.54 bohr above	$Y_D = 1.506$	[0, 1, −1] (i)	+0.37		**−1.59**		0		**−1.22**
tetrahedron edge	$\tilde{V}_D = 28.92$	[0, 1, 1]	−0.70		**+0.96**		0		**+0.26**
(C_{2v}^{x})	$\rho = 0.05209$	[1, 0, 0]	**−0.51**		+0.99		**−1.09**		**−0.61**
		type[c]	"{3, −1}"		"{3, +1}"				(3, −1)
		Laplacian	**−0.84**		+0.36		**−1.09**		**−1.58**
at 1.50 bohr above	$Y_D = 1.730$	2 x face (i)	**−0.19**		**−0.10**		0		**−0.29**
tetrahedron face	$\tilde{V}_D = 64.83$	radial	+0.83		+1.74		**−2.88**		**−0.31**
(C_{3v}^{xyz})	$\rho = 0.02668$	type[c]	"{3, −1}"		"{3, −1}"				(3, −3)
		Laplacian	+0.45		+1.54		**−2.88**		**−0.89**
at tetrahedron	$Y_D = 1.022$	all three	**+0.61**		**+0.14**		0		**+0.75**
center (T_d)	$\tilde{V}_D = 17.22$	type[c]	(3, +3)		(3, +3)				(3, +3)
	$\rho = 0.05938$	Laplacian	**+1.83**		**+0.42**		0		**+2.25**

[a] The dominating contributions for the sign of the corresponding ELI-D curvature or Laplacian within each row are marked in bold. [b] For each point considered the direction marked with "(i)" is parallel to the corresponding internuclear direction. [c] At each point the assigned bracket type of the rank/signature classification indicates, whether this point represents a critical point ("(r, s)" style) or not ("{r, s}" style) of the respective quantity electron density, pair-volume function, or ELI-D.

to the relative gradient vector components $(\ln \rho)'^{r}$ and $-(\ln \tilde{V}_D)'^{r}$ in radial direction (Figure 1c). Starting at the nucleus position with the well-known electron-nuclear cusp in the electron density,[18] there are no further critical points of $\rho(r)$ and $\tilde{V}_D(r)$ because they both behave strictly monotonically along r. With increasing r a sequence of ELI-D critical points marking the first-second shell boundary, the second shell maximum, the second-third shell boundary and the third shell maximum, respectively, are created at the crossings of the logarithmic derivative curves $\nabla \ln \rho$ and $-\nabla \ln \tilde{V}_D$ (eq 10b). A spatially bounded atomic shell as, e.g., the second shell of the Ar atom, is formed by the single wave type shape of $\nabla \ln \rho$ in this region. It crosses the less oscillating $-\nabla \ln \tilde{V}_D$ three times for each shell, at the two shell boundaries and at the shell's ELI-D maximum, whereas the spatially nonbounded valence region of the Ar atom displays only two critical points, the shell boundary and the attractor.

The Laplacian of ELI-D is decomposed into contributions from Hessian eigenvector directions in Figure 1d: the radial and tangential curvature contributions. For spherical symmetry the Laplacian of ELI-D reads

$$\nabla^2 Y_D^{\sigma}(\mathbf{r}) = \frac{\partial^2}{\partial r^2} Y_D^{\sigma}(\mathbf{r}) + \frac{2}{r}\frac{\partial}{\partial r} Y_D^{\sigma}(\mathbf{r}) \qquad \forall\ r \neq 0 \quad (23)$$

The first and the second term at the right hand side of eq 23 represents the radial and the sum of the two tangential curvatures of ELI-D, respectively. The zero-crossing of the radial curvature of ELI-D occurs where the ELI-D gradient magnitude attains a local maximum; i.e., it signals an ELI-D inflection point. This is generally valid for any symmetry. But from eq 23 there exists a relation between the tangential curvature $Y_D^{\sigma}{}''^{\mathrm{tt}}$ and the radial gradient $Y_D^{\sigma}{}'^{\mathrm{r}}$ of ELI-D for the case of spherical symmetry:

$$Y_D^{\sigma}{}''^{\mathrm{tt}} = \frac{1}{r} Y_D^{\sigma}{}'^{\mathrm{r}} \qquad \forall\ r \neq 0 \quad (24)$$

Therefore, the tangential ELI-D curvatures are equal to zero at those positions, where the radial ELI-D gradient equals zero, i.e., at an ELI-D critical point. Hence, all the ELI-D critical points besides the one at the origin are degenerate, displaying two zero tangential curvatures; i.e., they are either local maxima (1, −1) or minima (1, +1). Although for a spherical system eq 24 is valid at any point, for a molecular system the approximate validity of eq 24 in the valence region is a sign for the "local sphericity" of the ELI-D distribution.

With increasing distance from the nucleus the valence shell (and any other shell besides the first one) of a spherical atom always starts with positive ELI-D Laplacian, because the radial curvature dominates from the intershell minimum up to a certain point beyond. From eq 24 it is clear that the tangential curvatures equal zero at the intershell minimum, and they are positive up to the next shell maximum (where they are zero again) because ELI-D is increasing. Therefore, the point, where the ELI-D Laplacian starts getting negative, is located somewhere between the radial inflection point and the next shell maximum at larger r. Likewise, the point where the ELI-D Laplacian starts getting positive, is located somewhere between the radial inflection point and the next shell boundary at larger r. The valence shell maximum of ELI-D is followed by a radial inflection point and finally at larger distances (>5.3 bohr) the positive radial curvature dominates against the negative tangential ones leading to positive values of the ELI-D Laplacian approaching zero from above. As a rule, the Laplacian of ELI-D is negative in a region around the ELI-D maximum, and it is positive in a region around

the shell boundary. The occurrence of positive and negative ELI-D Laplacian for each ELI-D shell region Ω is implied by the definition of the intershell boundaries being surfaces of zero flux in ELI-D gradient. Therefore, the integral of the ELI-D Laplacian over each shell region vanishes:

$$\int_{\Omega} \nabla^2 Y_D^{\sigma}(\mathbf{r})\, d\mathbf{r} = \oint_{S_{\Omega}} \nabla Y_D^{\sigma}(\mathbf{r}) \cdot \mathbf{n}(\mathbf{r})\, dS = 0 \qquad (25)$$

where $\mathbf{n}(\mathbf{r})$ denotes the surface normal vector at position $\mathbf{r}$ of the ELI-D basin surface. Equation 25 is valid not only for the spherical shell case but also for any basin Ω of ELI-D. The argumentation based on Gauss' theorem is identical to the one given by Bader for the vanishing of the Laplacian of the density integral within each density basin.[2]

In Figure 1e the relative Laplacian of ELI-D is decomposed into components $\nabla^2\rho/\rho$, $\nabla^2\tilde{V}_D/\tilde{V}_D$, and $2\nabla \ln \rho \cdot \nabla \ln \tilde{V}_D$ according to eq 22. The relative density Laplacian displays the same oscillatory behavior with positive and negative values as the well investigated density Laplacian itself, and the zero axis crossings occur at the identical positions. Interestingly, $\nabla^2\tilde{V}_D/\tilde{V}_D$ does not display negative values at all. The mixed gradient term is negative everywhere, as can be verified from Figure 1b, where $\nabla \ln \rho$ and $\nabla \ln \tilde{V}_D$ are seen to display opposite sign everywhere along the line. This is consistent with expectations from eq 5.

5. Results for Diatomic Contact Situations

For a symmetrical diatomic molecule or an unbridged diatomic contact within a complex molecule the electron density typically displays local maxima (attractors) at the core positions and a (3, −1) critical point at the midpoint of the internuclear line. The single positive curvature of $\rho(\mathbf{r})$ at the (3, −1) critical point occurs for the internuclear direction, and the two perpendicular directions exhibit negative curvatures. Given the $\rho(\mathbf{r})$ curvatures at the (3, −1) saddle point, the pair-volume function is expected to qualitatively behave according to eq 18 revealing a (3, +1) critical point at the midpoint of the internuclear line. At the nuclear position the pair-volume function displays a local minimum. Typically, these topologies of the ELI-D constituents are observed for a large number of chemically quite different bonding situations. It is the competition between the different constituent terms (eqs 13 and 15) of the (relative) ELI-D curvature at the ELI-D critical point positions (determined by eqs 10), which characterizes the topology of the ELI-D scalar field. The Laplacian of ELI-D has been defined as a derived quantity of ELI-D to further characterize the ELI-D scalar field. It will be shown in the following that it serves to distinguish between different electronic situations with qualitatively similar ELI-D topologies.

To facilitate the discussion in the next chapters, a few naming conventions have to be introduced. The majority of the plots presented run along the internuclear line (INL). The discussion is mainly focused on the behavior of the various functions in the valence region as defined by ELI-D. In all the 1D-plots shown, the valence regions are indicated by a white background and the core regions display a gray background. The midpoint of the valence region along the internuclear line will be denoted INL-MV (internuclear line midpoint of valence region). Likewise for a triatomic interaction there can be defined an internuclear surface (INS) being the triangle whose edges are made from the three INLs. The midpoint of the valence region of this triangle is then denoted INS-MV.

Homopolar Single Bond: C_2H_6, Si_2H_6, Ge_2H_6. As the prototype case of a symmetrical single bond, the C−C bond in the molecule ethane is chosen. As can be seen from Figure 2b,c the behavior of ELI-D, $\rho(\mathbf{r})$ and $\tilde{V}_D(\mathbf{r})$ nicely illustrates the typical scenario mentioned before. The ELI-D critical point at the bond midpoint is created by the crossing of the $\nabla \ln \rho$ and $-\nabla \ln \tilde{V}_D$ curves, where the former displays a single wave shape and the latter is nearly constantly increasing in the valence region, i.e., between the two intershell saddle points. All three curvatures of ELI-D at the bond midpoint are negative, but for different reasons (Table 1a). For the bond direction the negative contribution from $\tilde{V}_D''/\tilde{V}_D$ exceeds the positive contribution from ρ''/ρ, whereas for the perpendicular (transverse) directions the negative contributions of ρ''/ρ dominate. Noticeably, comparison (Figure 2d) of the actual transverse curvature of ELI-D along the internuclear line with the one obtained from the spherical relationship between the transverse curvature and the longitudinal gradient (eq 24) reveals that the former behaves as in the spherical atom up to the position of the saddle point between the first and the second shell and starts to significantly deviate in the valence region due to the influence of the interatomic interaction. Interestingly, the same is true also for the bond-opposed side of the atom.

The Laplacian of ELI-D is negative not only at the ELI-D bond attractor but also for a certain region around it, e.g., for the larger part of the internuclear line in the valence region (Figure 2d). The latter is completely contained in the C−C bond attractor basin (not shown here) and due to eq 25 each ELI-D basin must contain compensating contributions of negative and positive ELI-D Laplacian values. The reason why it starts with positive values beyond the intershell boundary has already been discussed for the Ar atom and the same is true for C_2H_6.

It is instructive to perform a decomposition of the relative ELI-D Laplacian into pair-volume and density contributions (eq 22). It can be seen (Figure 2e) that both the Laplacian term of the density and that of the pair-volume function, provide sizable negative contributions to the negative Laplacian of ELI-D. This means that, within a region around the ELI-D attractor at bond midpoint $\nabla^2\tilde{V}_D/\tilde{V}_D$ is dominated by the one negative curvature parallel to the internuclear direction and $\nabla^2\rho/\rho$ is dominated by the two negative transverse curvatures (Table 1a). The latter behavior of the density Laplacian is well-known from many examples and provides the basis of Bader's classification of interatomic interactions into shared displaying negative density Laplacian and unshared (closed shell) ones with positive density Laplacian.[19] It is important to note that in the valence region, both $-\nabla^2\rho$ (not displayed here, but in ref 20) and $-\nabla^2\rho/\rho$ (Figure 2d) display two maxima along the internuclear line and the inclusion of the pair-volume function terms is necessary to reveal the place, where an electron is most localizable (in the sense of ELI[4]) along the interaction line in the valence region: at the ELI-D attractor located at the INL-MV.

To give an impression about the possible variations of ELI-D components in still classical homonuclear single bonds, the respective data for Si_2H_6 and Ge_2H_6 are displayed in Table 1b,c. The corresponding diagrams are depicted in Figure 2f−k (corresponding diagrams to Figure 2b,c are skipped, because they are very similar to the C_2H_6 case). Notable variations are the development of a double maximum structure of $-\nabla^2 Y_D^{\sigma}/Y_D^{\sigma}$ and $-\nabla^2 Y_D^{\sigma}$ for Si_2H_6 in contrast to the single maximum structure for the carbon and the germanium compound, and the systematic decrease of the transverse curvature of ELI-D at the attractor position. The latter observation will be discussed below (for N_2) in the context of distinguishing single from multiple bonds.

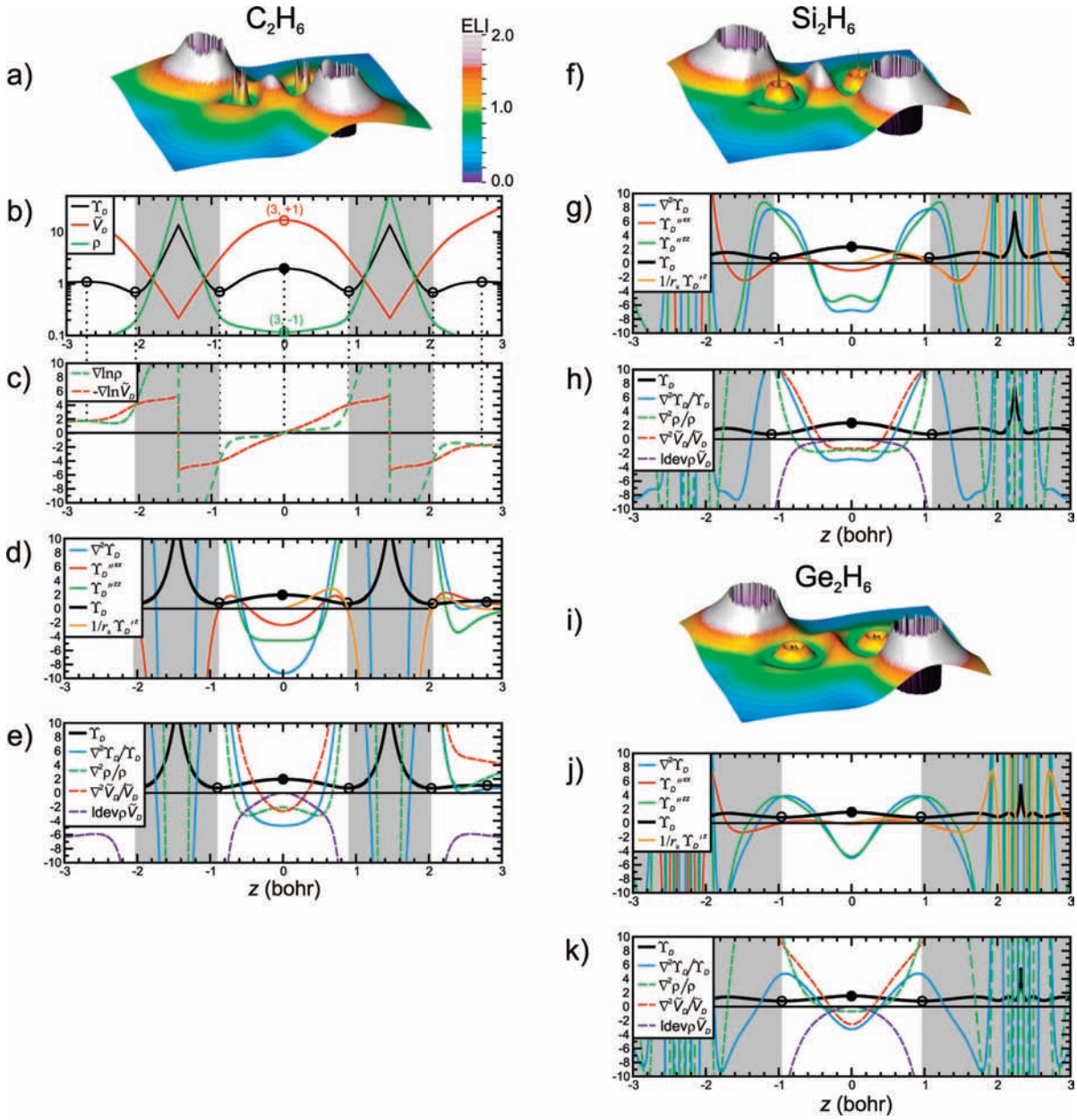

Figure 2. Molecules C_2H_6, Si_2H_6, Ge_2H_6: (a), (f), (i) ELI-D in combined height field/color map representation. Remaining diagrams: various quantities along internuclear line (z direction). Critical points are indicated with black filled spheres (attractors) and hollow circles. (b) Behavior (log scale) of ELI-D, $\tilde{V}_D$ and ρ. (c) behavior of $\nabla \ln \rho$ and $-\nabla \ln V_D$, ELI-D critical point formation (eq 10). (d), (g), (j) Laplacian of ELI-D, internuclear (z) and transverse (x) curvatures of ELI-D, "local sphericity" check ($1/r_a Y_D'^z$, eq 24). (e), (h), (k) Decomposition of relative ELI-D Laplacian (eq 22), $\mathrm{ldev}\rho\tilde{V}_D = 2\nabla \ln \rho \cdot \nabla \ln \tilde{V}_D$.

Homopolar Triple Bond: N_2 and C_2H_2. Because the double bond may be seen as only an intermediate situation to the cylindrical triple bond scenario, we skip the former and directly proceed to the latter. Concerning the triple bond scenario one exemplary case is represented by the N_2 molecule, which displays a (3, −3) critical point of ELI-D at the bond midpoint (Figure 3a). Similar to the single bond scenario, at the attractor position the negative ELI-D curvature in internuclear direction is caused by the dominance of the $\tilde{V}_D''/\tilde{V}_D$ term with the negative curvature of $\tilde{V}_D(\mathbf{r})$, and the negative curvatures in perpendicular directions are caused by the dominance of the ρ''/ρ term with the negative curvature of $\rho(\mathbf{r})$ (Table 1d).

Again, due to the prominent single-wave structure of $\nabla \ln \rho$ in the valence region between the atoms, and the simultaneously rather small variations of the slope of $-\nabla \ln \tilde{V}_D$ (Figure 3b,c), only one critical point of ELI-D is created, namely the attractor at bond midpoint. Of course, the Laplacian of ELI-D is negative there and, moreover, it creates an envelope in the valence region, which encompasses the bond attractor and the lone pair attractors in one connected domain of negative ELI-D Laplacian.

The small ELI-D curvature at INL-MV in the transverse direction signals a possible topological instability for this class of isoelectronic compounds and, unsurprisingly, a ring attractor surrounding the bond midpoint is displayed by C_2H_2 instead (Figure 3f). For this case, at the bond midpoint a (3, +1) critical point of ELI-D is displayed. Although the ELI-D triple bond topologies of N_2 and C_2H_2 are different, the regions of negative Laplacian of ELI-D are the same, because the (3, +1) critical point in C_2H_2 also displays a negative ELI-D Laplacian due to the strong dominance of the ELI-D curvature in internuclear direction (Table 1e). A topological instability between two chemically equivalent realizations of the triple bond in the

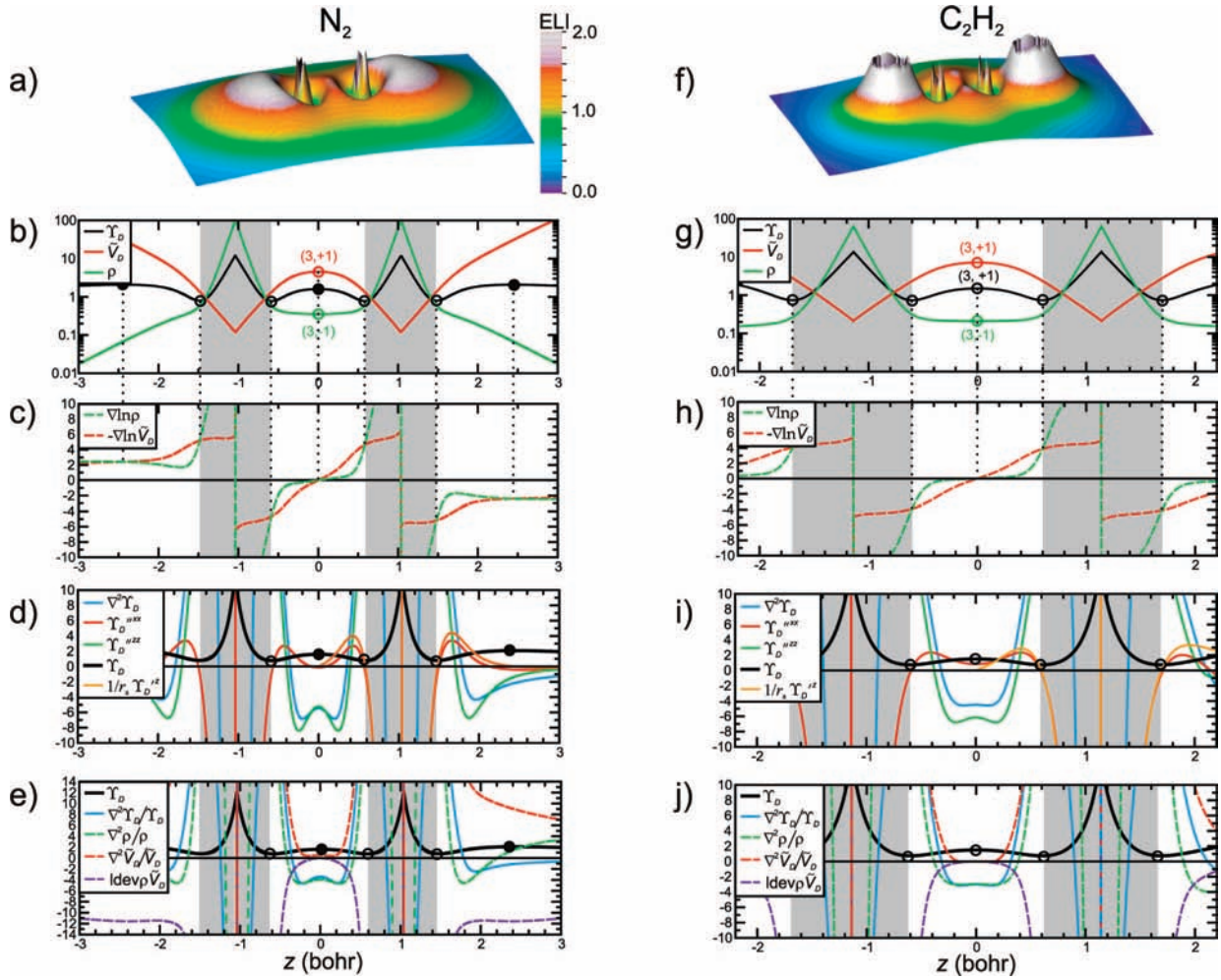

Figure 3. Molecules N_2, C_2H_2: (a), (f) ELI-D in combined height field/color map representation. Remaining diagrams: various quantities along internuclear line (z direction). Critical points are indicated with black filled spheres (attractors) and hollow circles. (b), (g) Behavior (log scale) of ELI-D, $\tilde{V}_D$ and ρ. (c), (h) Behavior of $\nabla \ln \rho$ and $-\nabla \ln \tilde{V}_D$, ELI-D critical point formation (eq 10). (d), (i) Laplacian of ELI-D, internuclear (z) and transverse (x) curvatures of ELI-D, "local sphericity" check ($1/r_a \Upsilon_D{}^{zz}$, eq 24). (e), (j) Decomposition of relative ELI-D Laplacian (eq 22), $\mathrm{ldev}\rho\tilde{V}_D = 2\nabla \ln \rho \cdot \nabla \ln \tilde{V}_D$.

framework of ELI-D (and ELF) is not related to thermodynamical instability.

A true challenge is the distinction between the single bond in Ge_2H_6 and the triple bond in N_2 on a topological basis because the curvatures of ELI-D are very comparable (cf. Table 1c vs 1d). The topological ellipticity of the electron density at the bond critical point, being defined as the ratio of the two tangential curvatures subtracted by 1, has been proposed as a measure of the π-character of a bond.[21] Because it only measures the deviation of the electron density at the bond critical point from cylindrical symmetry, for all axially symmetric molecules (including also Ge_2H_6 and N_2), its value at the bond critical point equals zero independent of the bond multiplicity. This is true not only for the electron density but also for the pair-volume function and ELI-D, which rules out the topological ellipticity as a suitable measure of bond multiplicity. However, inspection of the separate terms $\nabla^2\rho/\rho$ and $\nabla^2\tilde{V}_D/\tilde{V}_D$ of the relative ELI-D Laplacian (eq 22) for the single bonds in C_2H_6, Si_2H_6, and Ge_2H_6 (Table 1a−c) reveals significant negative contributions of both the electron density and the pair-volume Laplacian term at the ELI-D attractor position. In contrast, the negative relative Laplacian of ELI-D for N_2 and C_2H_2 is exclusively due to the negative contributions from $\nabla^2\rho/\rho$, and $\nabla^2\tilde{V}_D/\tilde{V}_D$ gives either positive or negligibly small negative contributions (Figure 3; Table 1d,e). Thus, there seems to be a clear distinction not only in Hilbert but also in real space between these two types of bonding. This opens an interesting perspective, whose general validity has to be further examined, of course.

Closed Shell Interaction: Ne_2. Having up to now analyzed bonding scenarios of single and triple bonds, it is instructive to compare with the chemically nonbonded situation obtained for a Ne_2 unit arbitrarily fixed at the interatomic distance in F_2. Although $\rho(\mathbf{r})$ and $\tilde{V}_D(\mathbf{r})$ possess the same topology as for N_2 (Figure 4b), $\nabla \ln \rho$ now displays a double-wave structure along the internuclear line in the valence region between the atoms, where it thus creates three critical points (Figure 4c). Analyzing the ELI-D (3, −1) critical point created at the INL-MV it can be seen from Table 1f that even (cf. C_2H_6, N_2) in the internuclear direction the density curvature term ρ''/ρ with large positive value strongly dominates yielding a positive internuclear curvature $Y_D^{\sigma}{}''/Y_D^{\sigma}$. Hence, the occurrence of an ELI-D critical point of type (3, −1) in the middle between the Ne atoms is caused by the dominance of the density curvature term ρ''/ρ not only in transverse directions but also in the internuclear direction.

Analyzing the relative ELI-D Laplacian $\nabla^2 Y_D^{\sigma}/Y_D^{\sigma}$ and its components (eq 22), one sees that there is a difference to the situations for the chemically bonded atoms. Interestingly, along the internuclear line (Figure 4e) $\nabla^2\tilde{V}_D/\tilde{V}_D$ behaves rather inconspicuously. Similar to the one for N_2, it displays a positive

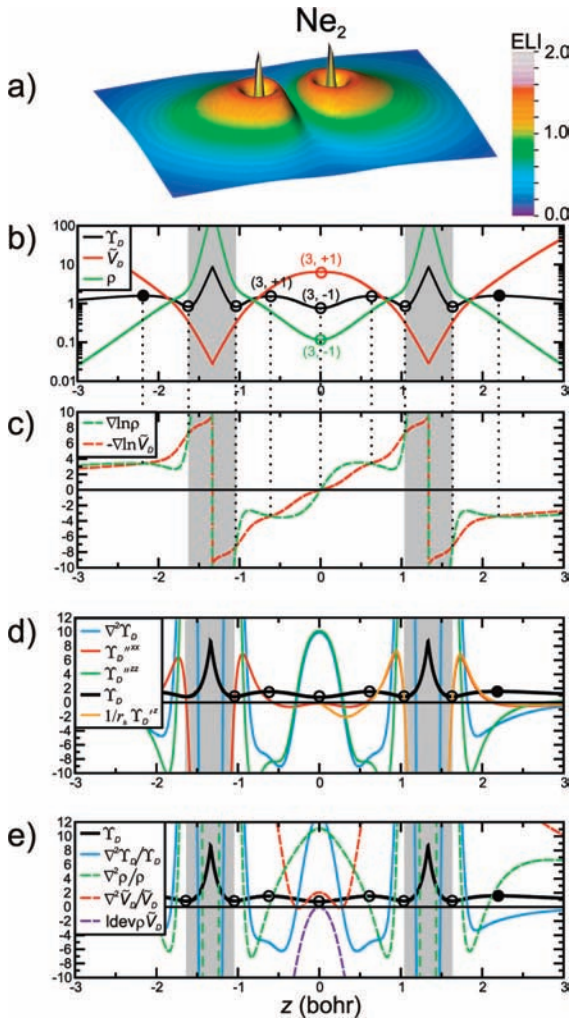

Figure 4. Unit Ne_2: (a) ELI-D in combined height field/color map representation. Remaining diagrams: various quantities along internuclear line (z direction). Critical points are indicated with black filled spheres (attractors) and hollow circles. (b) Behavior (log scale) of ELI-D, $\tilde{V}_D$ and ρ. (c) Behavior of $\nabla \ln \rho$ and $-\nabla \ln \tilde{V}_D$, ELI-D critical point formation (eq 10). (d) Laplacian of ELI-D, internuclear (z) and transverse (x) curvatures of ELI-D, "local sphericity" check ($1/r_a Y_D'^z$, eq 24). (e) Decomposition of relative ELI-D Laplacian (eq 22), $\mathrm{ldev}\rho\tilde{V}_D = 2\nabla \ln \rho \cdot \nabla \ln \tilde{V}_D$.

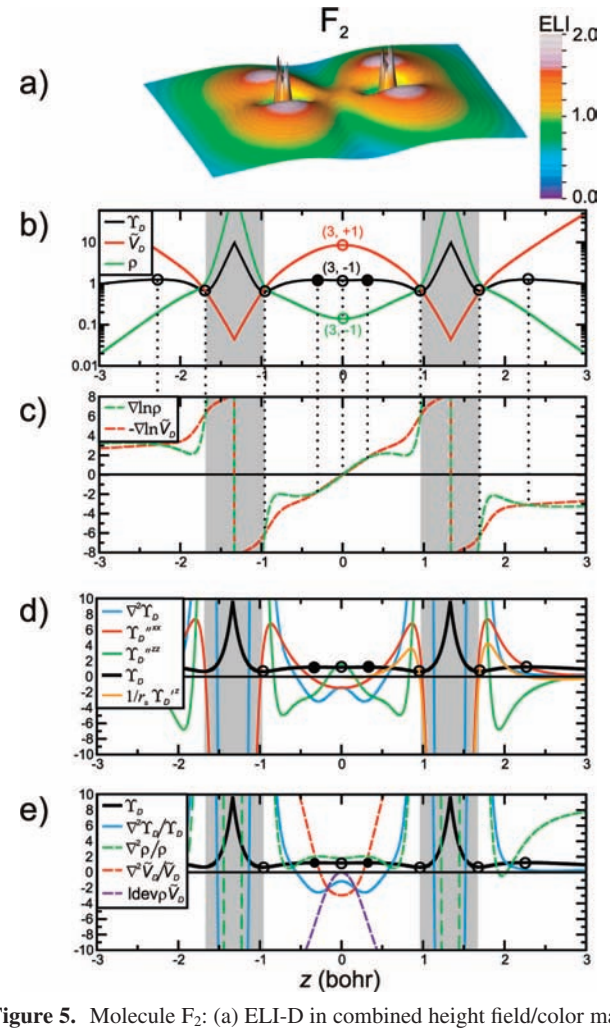

Figure 5. Molecule F_2: (a) ELI-D in combined height field/color map representation. Remaining diagrams: various quantities along internuclear line (z direction). Critical points are indicated with black filled spheres (attractors) and hollow circles. (b) Behavior (log scale) of ELI-D, $\tilde{V}_D$ and ρ. (c) Behavior of $\nabla \ln \rho$and $-\nabla \ln \tilde{V}_D$, ELI-D critical point formation (eq 10). (d) Laplacian of ELI-D, internuclear (z) and transverse (x) curvatures of ELI-D, "local sphericity" check ($1/r_a Y_D'^z$, eq 24). (e) Decomposition of relative ELI-D Laplacian (eq 22), $\mathrm{ldev}\rho\tilde{V}_D = 2\nabla \ln \rho \cdot \nabla \ln \tilde{V}_D$.

maximum at the interatomic midpoint, which is due to dominating positive transverse curvature contributions. Turning to the electron density, one can see (Table 1f) that at the interatomic midpoint the already mentioned large positive ρ''/ρ contribution in internuclear direction heavily dominates $\nabla^2\rho/\rho$, which itself dominates the Laplacian of ELI-D. In contrast to all the other bonding scenarios discussed before, the Laplacian of ELI-D is strongly positive at the interatomic midpoint and even in a large region between the atoms (Figure 4e). The two Ne atoms are located in two clearly separated domains of negative ELI-D Laplacian. This is a novel and clear signature of a closed shell interaction in the framework of ELI-D topology.

Case of F_2. To elucidate the value of this novel finding, a more difficult example of diatomic bonding is analyzed: in contrast to all classical covalently bonded molecules analyzed before, the molecule F_2 displays a double maximum structure of ELI-D (at DFT and correlated level of theory[6]) in the valence region along the internuclear line. Noteworthy, $\rho(\mathbf{r})$ and $\tilde{V}_D(\mathbf{r})$ have the same topology as for N_2 and Ne_2 (Figure 5b). The comparably rather steep (cf. C_2H_6, N_2) $\nabla \ln \rho$ curve along the internuclear line displays a very shallow double-wave structure in the valence region, which leads in the valence region to three critical points along the internuclear line (Figure 5c). At the bond midpoint (INL-MV) all three quantities display critical points, namely (3, −1) and (3, +1) critical points for $\rho(\mathbf{r})$ and $\tilde{V}_D(\mathbf{r})$, respectively, and a (3, −1) critical point for ELI-D.[6] This already means that at the bond midpoint the ρ''/ρ term dominates the relative ELI-D curvatures $Y_D^{\sigma}''/Y_D^{\sigma}$ in all three main axis directions (Table 1g) as was found for Ne_2. However, the behavior of the relative Laplacian terms is different from the Ne_2 case: the $\nabla^2\tilde{V}_D/\tilde{V}_D$ term displays the typical shape seen above for single bonds with negative values in the region of the bond midpoint. The density Laplacian is positive (also in our MRCI calculations) as for Ne_2, but the $\nabla^2\rho/\rho$ term does not dominate $\nabla^2 Y_D^{\sigma}/Y_D^{\sigma}$. The negative values of $\nabla^2 Y_D^{\sigma}/Y_D^{\sigma}$ in the bonding region are due to the $\nabla^2\tilde{V}_D/\tilde{V}_D$ and $2\nabla \ln \rho \cdot \nabla \ln \tilde{V}_D$ terms (Figure 5e). At the bond midpoint, where the latter has no contributions due to symmetry, $\nabla^2\tilde{V}_D/\tilde{V}_D$ dominates the relative ELI-D Laplacian due to large negative $\tilde{V}_D''/\tilde{V}_D$ contributions in internuclear direction (Table 1g). In the region of the ELI-D attractors and closer to the shell boundary the $2\nabla \ln \rho \cdot \nabla \ln \tilde{V}_D$ term dominates. With all the examples analyzed up to now in mind, the $2\nabla \ln \rho \cdot \nabla \ln \tilde{V}_D$ term can be classified

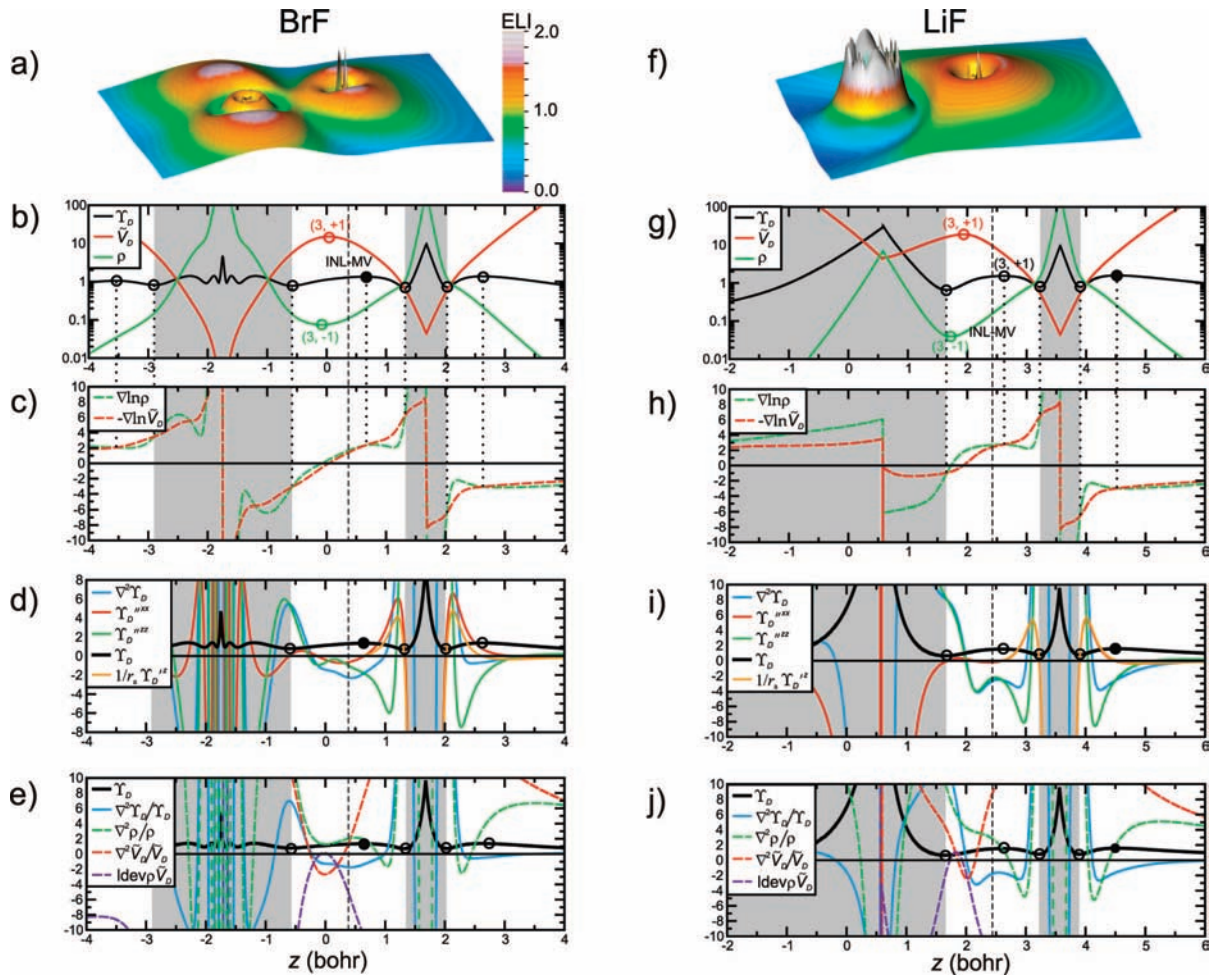

Figure 6. Molecules BrF, LiF: (a), (f) ELI-D in combined height field/color map representation. Remaining diagrams: various quantities along internuclear line (z direction). Critical points are indicated with black filled spheres (attractors) and hollow circles. (b), (g) Behavior (log scale) of ELI-D, $\tilde{V}_D$ and ρ. (c), (h) Behavior of $\nabla \ln \rho$ and $-\nabla \ln \tilde{V}_D$, ELI-D critical point formation (eq 10);. (d,) (i) Laplacian of ELI-D, internuclear (z) and transverse (x) curvatures of ELI-D, "local sphericity" check ($1/r_a Y_D{}'^z$, eq 24). (e), (j) Decomposition of relative ELI-D Laplacian (eq 22), $\mathrm{ldev}\rho\tilde{V}_D = 2\nabla \ln \rho \cdot \nabla \ln \tilde{V}_D$.

to behave rather unspecific with respect to the bonding situation, because it is found typically negative between the atoms with large contributions around to the shell boundary; i.e., the behavior of $2\nabla \ln \rho \cdot \nabla \ln \tilde{V}_D$ along the internuclear line is qualitatively the same for all the molecules investigated.

For the molecule Cl_2 (not shown here) an ELI-D attractor is found at the bond midpoint and the homonuclear bonding scenario is somewhat in-between that of F_2 and C_2H_6: unlike in F_2 it displays negative $\nabla^2\rho/\rho$ contributions in the region around the bond midpoint, however in a strongly reduced amount compared to C_2H_6. Similar to F_2 the negative $\nabla^2\tilde{V}_D/\tilde{V}_D$ term dominates at the bond midpoint due to sizable $\tilde{V}_D''/\tilde{V}_D$ contributions in internuclear direction.

Thus, the variable behaviors of $\nabla^2\rho/\rho$ and $\nabla^2\tilde{V}_D/\tilde{V}_D$ discriminate between the single bond scenarios for C_2H_6, Cl_2, and F_2 and also between those and the triple bond scenario in N_2.

Polar Bonding: BrF, LiF. One further aspect of diatomic bonding is the occurrence of just a single ELI-D attractor along the internuclear line, but which is shifted significantly away from the INL-MV as it is typically found for heteropolar bonding situations. As the first example, the molecule BrF is chosen. The curves of the logarithmic derivatives $\nabla \ln \rho$ and $-\nabla \ln \tilde{V}_D$ along the internuclear line are displayed in Figure 6c. It can be seen that the critical points of ρ and $\tilde{V}_D$ are both displaced from the INL-MV toward the Br atom. The critical point of $\tilde{V}_D$ lies closer to the more electronegative F atom than the one for ρ, which seems to be a rather general behavior also found for other examples not discussed here. The noncoincidence of the density and the pair-volume function critical points (with a distance of 0.12 bohr) marks already a significant deviation from the zeroth-order estimated relation between the two (eq 5). This has important consequences: the creation of the ELI-D attractor as described by eqs 10 takes place significantly apart from the INL-MV. The reason is the quite parallel course of $\nabla \ln \rho$ and $-\nabla \ln \tilde{V}_D$ in the region of the INL-MV, such that their intersection and the creation of an ELI-D (3, −3) critical point takes place about +0.3 bohr apart from it (Figure 6c) in the vicinity of the F first shell boundary. Due to the proximity of the attractor to the F atom shell boundary another peculiarity appears. From Table 1h it can be seen that different from the examples given until now, at the ELI-D attractor position the $\tilde{V}_D''/\tilde{V}_D$ contribution to the relative ELI-D curvature displays a positive value also in the internuclear direction. This is caused by the location of the ELI-D attractor beyond the internuclear inflection point of the pair-volume function, whose internuclear curvature is indeed negative around the INL-MV (see Table 1h) as expected but no longer in the vicinity of the ELI-D attractor. At the ELI-D attractor position the negative relative curvature of ELI-D in internuclear direction is solely produced

by the large negative values from the $2(\ln \rho)'(\ln \tilde{V}_D)'$ term, which dominates over positive contributions from $\tilde{V}_D''/\tilde{V}_D$ and ρ''/ρ.

Likewise, the negative values of the relative Laplacian of ELI-D at the INL-MV and at the ELI-D attractor are caused by the large negative values from the $2\nabla \ln \rho \cdot \nabla \ln \tilde{V}_D$ term dominating over positive values from the $\nabla^2 \tilde{V}_D/\tilde{V}_D$ and $\nabla^2\rho/\rho$ terms (Figure 6e).

Thus, similar to F_2 the creation of the ELI-D attractor apart from the INL-MV in the vicinity of the shell boundary of the fluorine atom causes the unspecific (as mentioned before) $2\nabla \ln \rho \cdot \nabla \ln \tilde{V}_D$ term to dominate the relative ELI-D Laplacian against positive contributions of the $\nabla^2\rho/\rho$ and $\nabla^2\tilde{V}_D/\tilde{V}_D$ terms (Figure 6e). In contrast to F_2, at the ELI-D attractor the $\tilde{V}_D''/\tilde{V}_D$ term yields positive contributions in internuclear direction, a peculiarity not been observed for any molecule discussed before. Because the distance of the ELI-D attractor from the F atom is very much the same in F_2 ($d = 1.02$ bohr) and BrF ($d = 1.05$ bohr), this different behavior of the internuclear pair-volume function curvature is caused by the different chemical bonding. For the more covalent molecule F_2, the ELI-D attractor lies within the region, where the pair-volume function curvature in internuclear direction still displays the same (negative) sign as at the (3, +1) saddle point of the pair-volume function, whereas for BrF it still displays the initially positive sign from starting at the F core.

Turning to the analysis of "locally spherical behavior" of the ELI-D transverse curvature along the internuclear line, it can be noticed (Figure 6d) that, starting from the intershell saddle point of the F atom at the bond directed side, a significant deviation occurs between the transverse ELI-D curvature and the longitudinal ELI gradient term (eq 24). The deviation goes back to zero roughly at the position of the ELI-D attractor, where the gradient term necessarily and the transverse curvature nearly adopts zero value. Actually, the displacement of the respective zero axis crossings is only about 0.01 bohr. This is a significant difference to F_2, where the corresponding displacement already amounts to about 0.08 bohr.

All this may be seen as signatures of the polar covalent bond in the present context of ELI-D decomposition. Finally, it is to be noted that also for this example of a polar covalent bond a common region of negative ELI-D Laplacian surrounds both atoms.

A further example of a heteropolar bonding situation is represented by the molecule LiF. From chemical bonding concepts there exists a difference between heteronuclear bonding in BrF and LiF, because in the former each atom may achieve an electronic noble gas configuration via ideal electron sharing, whereas in the latter an octet configuration is only possible via ideal charge transfer from Li to F. So, although BrF might be considered an example for a polarized bond, LiF could be expected to be an example of a polar bond in the sense of a contact ion pair. For the two cases the topologies of ELI-D are different giving a (3, −3) attractor on the internuclear line close to the F atom for BrF (described above) and a ring attractor with an associated (3, +1) saddle point close to the F atom for LiF. The Laplacian of ELI-D is negative even (one negative curvature competes with two positive curvatures) at the (3,+1) point, and its constituent quantities behave similar to BrF (Figure 6j). This is documented numerically also in Table 1i. However, one significant difference can be found: the transverse component of ELI-D curvature behaves for LiF in the locally spherical way (eq 24) from the F nucleus up to the (3, +1) saddle point in the valence region (Figure 6i), whereas for BrF it already starts to deviate beyond the F first shell (Figure 6d). This difference has been verified for ClF, LiCl and NaCl as well.

6. Results for Ring-Shaped Molecules: C_6H_6 and C_3H_6

It is instructive to analyze the topology of ELI-D for simple ring-type molecules, because they represent in two dimensions also a prototype scenario for certain cage molecules. We choose benzene with six bond attractors in the molecular plane as first example (Figure 7a). The two different positions to be analyzed are those of the ELI-D attractor position and the ring midpoint. Due to symmetry only at the ring midpoint (point group $D_{6h}{}^z$) the critical points of $\rho(\mathbf{r})$, $\tilde{V}_D(\mathbf{r})$ and ELI-D exactly coincide. At the INL-MV position none of the three quantities displays a critical point; however, the displacements ("+" sign, exocyclical; "−" sign, endocyclical direction) of the respective critical points from the ideal geometrical position are so small ($\rho(\mathbf{r})$, +0.003 bohr; $\tilde{V}_D(\mathbf{r})$, −0.010 bohr; ELI-D, +0.016 bohr) that it does not play a role in the present discussion (Figure 7b). This can be verified from Table 1j, where the $2(\ln \rho)'(\ln \tilde{V}_D)'$ term (along y direction for the point selected) at the ELI-D attractor is vanishingly small and the curvatures of $\rho(\mathbf{r})$ and $\tilde{V}_D(\mathbf{r})$ exhibit the same characteristics at the ELI-D critical point as if they had a critical point themselves at that position. Thus, slightly displaced from the INL between two neighbouring C atoms an ELI-D attractor is found, and the curvatures of $\rho(\mathbf{r})$ and $\tilde{V}_D(\mathbf{r})$ display the typical behavior as discussed before: the electron density displays a (3, −1)-type of behavior, the pair-volume function a (3, +1)-type of behavior. The $\tilde{V}_D''/\tilde{V}_D$ term dominates in internuclear direction, resulting in a negative curvature of ELI-D, whereas in the perpendicular directions the negative contributions from the ρ''/ρ term dominate. In total, this leads to a corresponding ELI-D attractor between the atoms. As expected from the foregoing discussion about the behavior of the pair-volume function for multiple bonds, the contribution from the $\nabla^2\tilde{V}_D/\tilde{V}_D$ term is negative but displays only half the value of the $\nabla^2\rho/\rho$ term. Roughly, this behavior is situated between the single and the triple bond scenario.

The ring midpoint represents a new type of topological situation, because an equal influence of six atoms is responsible for the characteristics. The electron density displays a (3, +1) critical point there, with two positive curvatures within the molecular plane, and $\tilde{V}_D(\mathbf{r})$ a (3, −1) critical point, with two negative curvatures within the plane (Table 1j). These findings are typical for a ring type arrangement of atoms. In the case of benzene the ring midpoint displays a (3, +1) critical point of ELI-D, which means that the ρ''/ρ term dominates in all three main axis directions.

This typical behavior of $\rho(\mathbf{r})$ and $\tilde{V}_D(\mathbf{r})$ at the ring midpoint does not change even in the case of the smallest C ring in cyclopropane, where ρ and ρ'' display larger and $\tilde{V}_D$ and $\tilde{V}_D''$ display smaller value magnitudes than for benzene (Table 1k), which is expected already from the smaller ring size. However, the actual values of the ratios ρ''/ρ and $\tilde{V}_D''/\tilde{V}_D$ change differently: the curvature terms within the (x, y) molecular plane are found decreased, but they are found increased in z direction.

Interestingly, due to the short distance of the INL-MV to the transannular C atom the behavior along the INL changes remarkably. The critical points of $\rho(\mathbf{r})$ and $\tilde{V}_D(\mathbf{r})$ are significantly displaced from the INL-MV in a perpendicular direction to the INL. The situation is displayed in Figure 7f. The (3, −1) point of $\rho(\mathbf{r})$ lies only very slightly ($d = +0.07$ bohr) displaced in the exocyclic region, whereas the (3, +1) point of $\tilde{V}_D(\mathbf{r})$ is strongly displaced in the opposite direction ($d = -0.52$ bohr), i.e., inside the ring, with the ring midpoint located at $d = -0.83$

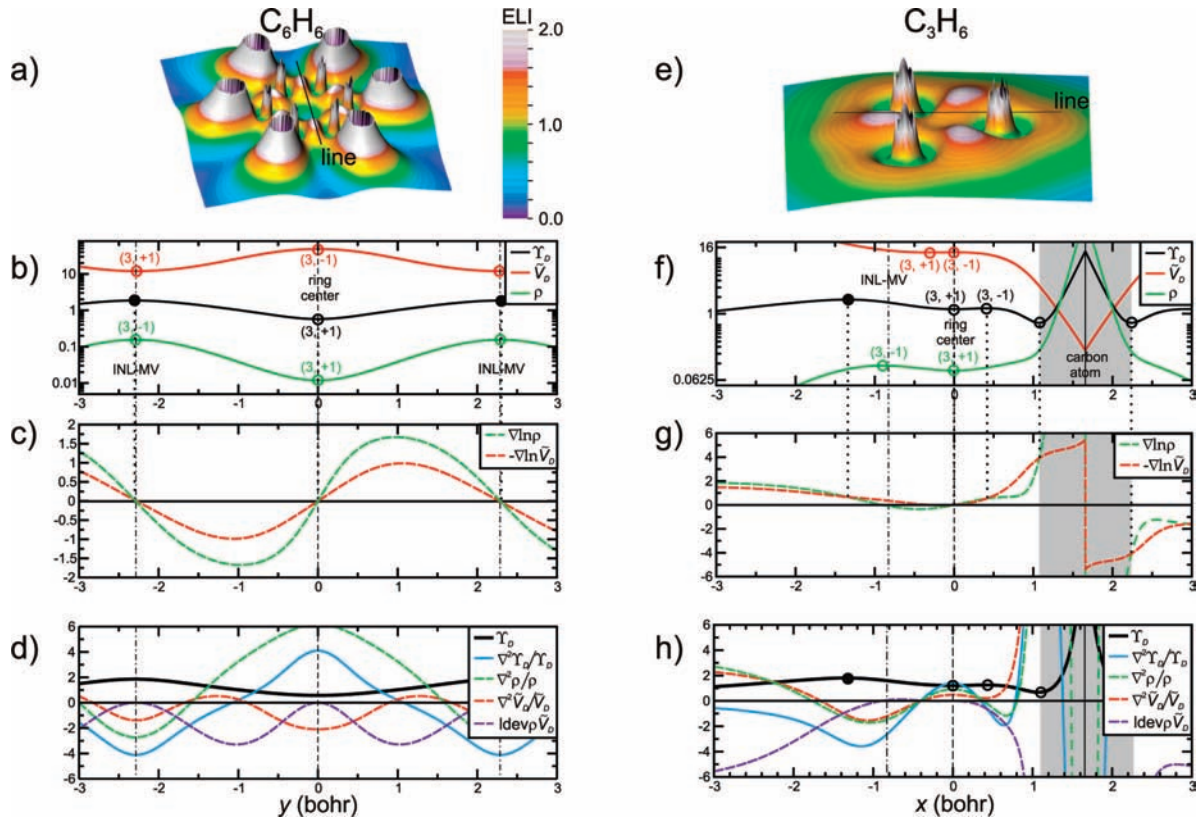

Figure 7. Molecules C_6H_6, C_3H_6: (a), (e) ELI-D in combined height field/color map representation. Remaining diagrams: various quantities along a line (drawn in (a) and (e)) through the ring center and the midpoint of two and one ring edges (INL-MV) for C_6H_6 and C_3H_6, respectively. Critical points are indicated with black filled spheres (attractors) and hollow circles. (b), (f) Behavior (log scale) of ELI-D, $\tilde{V}_D$ and ρ. (c), (g) Behavior of $\nabla \ln \rho$ and $-\nabla \ln \tilde{V}_D$, ELI-D critical point formation (eq 10). (d), (h) Decomposition of relative ELI-D Laplacian (eq 22), $\mathrm{ldev}\rho\tilde{V}_D = 2\nabla \ln \rho \cdot \nabla \ln \tilde{V}_D$.

bohr from the INL-MV. As a result, the creation of the ELI-D attractor due to eqs 10 takes place in the exterior region at $d = +0.52$ bohr displaced from the INL-MV (Figure 7g). Thus, in cyclo-C_3H_6 the origin of the sizable displacement of the local maximum of electron localizability from the INL-MV is the pair-volume function contribution from the bond-opposed C atom. This is not at variance with the traditional interpretation of a bent-bond scenario as a signature of ring strain.

Turning to the Laplacian of ELI-D distributions for these 2-center bonded ring-shaped molecules, it is to be noticed that the atomic skeleton is totally contained in a common region of negative Laplacian of ELI-D, and the center region of the ring is excluded displaying positive values (Figure 7d,h) spreading along the z direction, such that the region of positive ELI-D Laplacian is not just a bubble.

If, for another symmetrical ring-type molecule, there happens to be a multicenter bonding situation with an ELI-D attractor at ring midpoint, the Laplacian of ELI-D necessarily must be negative there, too. In detail, the $\tilde{V}_D''/\tilde{V}_D$ term then has to dominate in the bonding directions, i.e., within the plane, and the ρ''/ρ term dominates in direction perpendicular to the plane.

7. Results for Cage Situations: C_4H_4, B_4H_4

Turning to cage situations, a few expectations from the foregoing discussion can already be formulated. In the case of regular convex polyhedra, with faces made from equilateral triangles and where the interfacial angles (angles between normal vectors) are sufficiently large like in the tetrahedron and the octahedron, it can be expected that in classical 2-center−2-electron bonding situations ELI-D attractors are located above the edges of the polyhedron. This situation is analyzed in detail for the tetrahedrane molecule C_4H_4 with tetrahedral symmetry (Figure 8, Table 1l). The radial displacement of the ELI-D attractor from the INL-MV to the exterior region of the polyhedron above the edge results from the same mechanism as for C_3H_6: the radial displacement of the density and pair-volume function critical points, the former slightly to outside the polyhedron, the latter significantly to the inside (Figure 8b). It can be seen (Table 1l) that at the ELI-D attractor the different curvatures of $\rho(\mathbf{r})$ and $\tilde{V}_D(\mathbf{r})$ display the expected (3, −1) and (3, +1) type of behavior, respectively, although only ELI-D has a critical point there. In the displacement direction ([1, 0, 0] in Table 1l) the $2(\ln \rho)'(\ln \tilde{V}_D)'$ term has the dominating negative contributions to the ELI-D curvature, as for C_3H_6.

Because each tetrahedron face is opposed by a close-lying vertex (at distance $d = 0.82\ d(\mathrm{C-C})$), it can now be expected that the ELI-D critical point associated with the triangular face should be located significantly above the faces although the related electron density critical point is only slightly displaced. For tetrahedrane the ELI-D critical point above the face is of type (3, +1) and it is displaced from the face midpoint by +0.57 bohr in face normal direction, whereas the density critical (3, +1) point is displaced only by +0.07 bohr (Figure 8e). Interestingly, the distance from the triangular face atoms to the ELI-D (3, +1) critical point is nearly the same as from the atoms to the tetrahedron midpoint. The topological decomposition of ELI-D is given in Table 1l. It can be seen that the ELI-D curvatures at the face critical point are very similar to those in C_3H_6. For the relative ELI-D curvature in the face normal direction (denoted

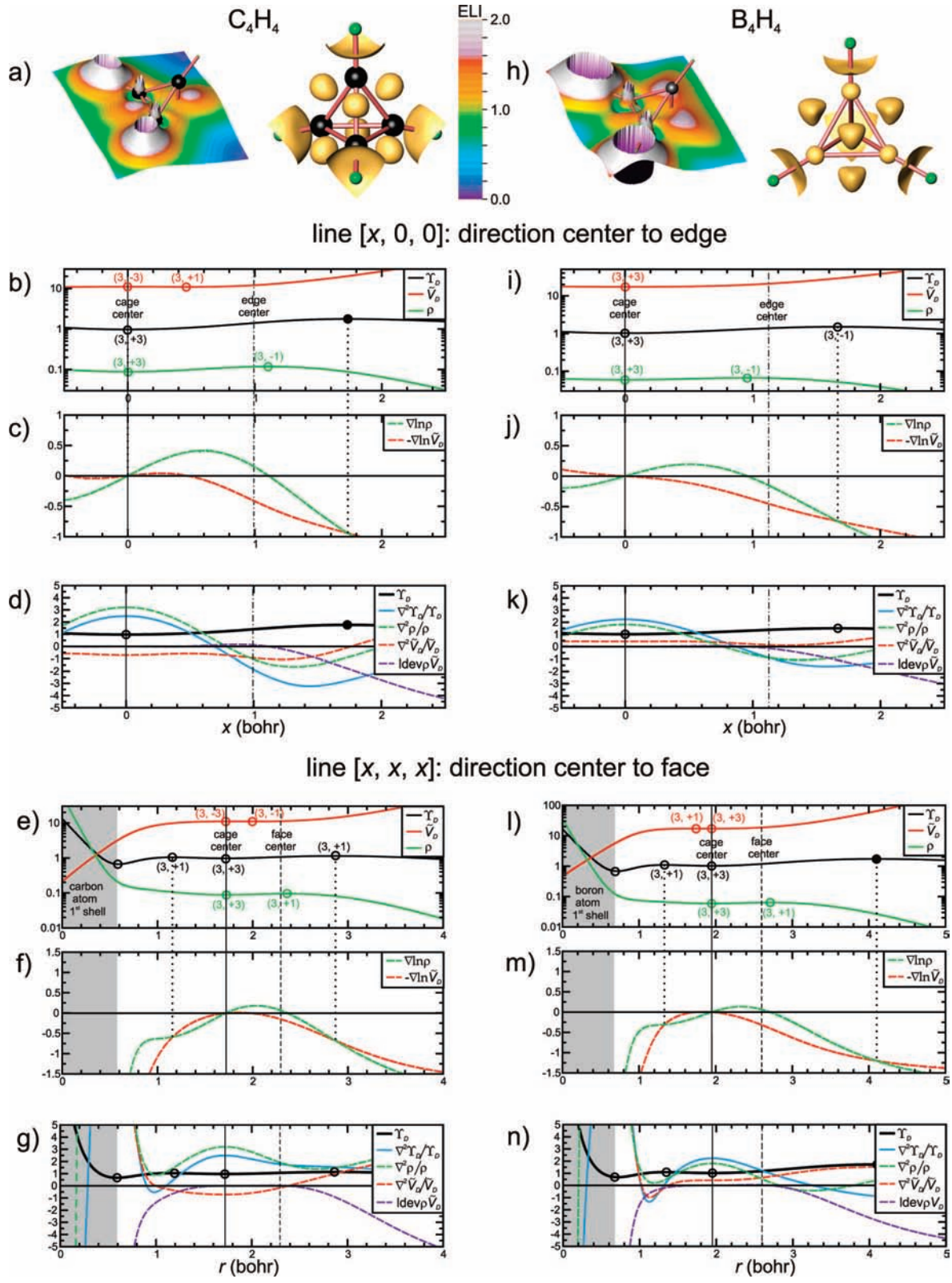

Figure 8. Molecules C_4H_4, B_4H_4: (a), (h) ELI-D in combined height field/color map representation and ELI-D isosurface representation. Remaining diagrams: various quantities along lines containing the tetrahedron center and the midpoint of the tetrahedron edge and lines containing the tetrahedron center and the midpoint of the tetrahedron face, respectively. Critical points are indicated with black filled spheres (attractors) and hollow circles. (b), (e), (i), (l) Behavior (log scale) of ELI-D, $\tilde{V}_D$ and ρ. (c), (f), (j), (m) Behavior of $\nabla \ln \rho$ and $-\nabla \ln \tilde{V}_D$, ELI-D critical point formation (eq 10). (d), (g), (k), (n) Decomposition of relative ELI-D Laplacian (eq 22), $\mathrm{ldev}\rho\tilde{V}_D = 2\nabla \ln \rho \cdot \nabla \ln \tilde{V}_D$.

"radial" in Table 1l) the sizable negative contribution from the $2(\ln \rho)' (\ln \tilde{V}_D)'$ term is to be noted, which is zero at the ring center in C_3H_6. Only together with the decreased (cf. C_3H_6, Table 1k) ρ''/ρ term with negative contributions do they dominate over the very similar (cf. C_3H_6, Table 1k) $\tilde{V}_D''/\tilde{V}_D$ term of positive sign.

At the tetrahedron midpoint the critical points of ρ, $\tilde{V}_D$ and ELI-D coincide. The corresponding curvature terms behave as

expected displaying a (3, +3) critical point of ρ, a (3, −3) critical point of $\tilde{V}_D$ and a (3, +3) critical point of ELI-D due to complete dominance of the density curvature term.

The relative Laplacian of ELI-D displays a region of negative values that includes the whole molecular graph but that leaves out the face center and cage center regions displaying positive values (Figure 8d,g).

Turning to closo-tetraborane B_4H_4 with ELI-D attractors above the faces, it is now interesting to analyze the differences to C_4H_4. With an interatomic distance of $d(B-B) = 3.18$ bohr the cage is significantly enlarged compared to $d(C-C) = 2.81$ bohr for C_4H_4. The expected ring critical (3, +1) point of the electron density is at +0.11 bohr above the face, but at the ELI-D attractor position located 1.50 bohr above the face (Figure 8l) the signs of ρ'' have completely changed and unexpectedly display negative curvatures for the facial (tangential) directions (Table 1m). The reason is that the ELI-D attractor is located beyond the inflection point for the tangential density curvature. This is different from C_4H_4, where the ELI-D face critical point lies within the positive tangential ρ curvature domain, and even at larger distances from the face a negative tangential ρ curvature is not displayed. Thus, this feature for B_4H_4 is specific for the bonding situation, at least as displayed by the method of calculation used. For an ELI-D attractor to occur above the face a (3, −1) type of behavior of the density at the ELI-D critical point position might be quite important for the actual case, because only then there is no competition between the small negative $\tilde{V}_D''/\tilde{V}_D$ and ρ''/ρ term in tangential directions (Table 1m). At the actual ELI-D attractor location the negative contributions of the density curvature term even exceed those of the pair-volume curvature term by a factor of 2. If the ELI-D critical point were located closer to the face, such that the tangential components of ρ''/ρ were positive, they could easily dominate the ELI-D curvature in these directions and a (3, +1) critical point of ELI-D above the face would result.

At the tetrahedron center the occurrence of a (3, +3) critical point of the pair-volume function is unexpected, but it has no influence on the topology of ELI-D there. It additionally provides a small positive contribution to the already much larger positive ρ''/ρ contributions such that the (3, +3) type of the ELI-D critical point is not in any danger to change the signature.

Comparison of the ELI-D Laplacian distribution with that of C_4H_4 reveals a significant difference: for B_4H_4 the domain of negative relative ELI-D Laplacian additionally encompasses a region above the tetrahedron face (Figure 8n). The central cage region still displays positive relative ELI-D Laplacian as for C_4H_4.

8. Discussion

The quantity ELI-D, derived from the same-spin pair density can be shown to be directly related to the event probability that a single electron is alone in a given spatial region of D-restricted partitioning. Its value is connected with the local pairing avoidance of same-spin electrons. In this sense it represents a measure of electron localizability. ELI-D can be given as a simple product of a 1-particle and a 2-particle quantity, the density and the pair-volume function, respectively. In the previous section the interplay of the electron density and the pair-volume function with respect to the creation of characteristic ELI-D topologies has been analyzed for a number of different chemical bonding situations.

There is a typical topology of the electron density and the pair-volume function for different dimensionalities of interatomic interaction. The occurrence of (3, −1) bond critical, (3, +1) ring critical, and (3, +3) cage critical points, respectively, of the electron density has been discussed in depth by Bader.[2] The curvature of the electron density at a density critical point is typically positive in internuclear and negative in transverse direction.[2] As shown above, the pair-volume function has a related topology. In good agreement with a simple zeroth-order estimate the two functions have been found to typically display mutually opposite behavior in position space; i.e., their gradients typically possess mutually opposite signs. Moreover, at critical points of ELI-D it is found that the corresponding curvatures of the density and the pair-volume function typically display opposite signs in the directions of the ELI-D Hessian eigenvectors. Exceptions seem to be rare (e.g., B_4H_4) but represent especially interesting bonding scenarios in the framework of ELI-D, because they are mainly found where the critical points of the electron density and the pair-volume function are pronouncedly displaced from the ELI-D one.

For a given type of critical point scenario of the density and the pair-volume function, different types of ELI-D topology may occur. The actual type of ELI-D critical point is determined by the signs of the respective ELI-D curvatures of the diagonalized Hessian matrix. In each eigenvector direction, the sign of the ELI-D curvature is determined by the competition between the terms $\tilde{V}_D''/\tilde{V}_D$, ρ''/ρ, and $2(\ln \rho)'(\ln \tilde{V}_D)'$. Thus, for three negative ELI-D curvatures at an ELI-D critical point to occur, the $\tilde{V}_D''/\tilde{V}_D$ term (plus the mixed logarithmic derivative term) must dominate the internuclear direction(s), and the ρ''/ρ term (plus the mixed logarithmic derivative term) must dominate the transverse direction(s). The $2(\ln \rho)'(\ln \tilde{V}_D)'$ term supports negative ELI-D curvatures, because in any direction it is strictly negative or at most zero at an ELI-D critical point. It typically adopts a maximal value (least negative value) between the location of two close density and the pair-volume function critical points and rather steeply decreases away from it. Thus, if the location of the ELI-D attractor is far away from the critical points of the electron density and the pair-volume function, the $2(\ln \rho)'(\ln \tilde{V}_D)'$ term typically displays large negative contributions, which are then competitive with $\tilde{V}_D''/\tilde{V}_D$ and ρ''/ρ term contributions to the respective curvature of ELI-D. Moreover, $2(\ln \rho)'(\ln \tilde{V}_D)'$ may even yield dominant contributions to the relative Laplacian of ELI-D. This situation has been found for the molecule LiF.

The analysis of "local sphericity" of an ELI-D distribution with the aid of the transverse ELI-D curvature allows distinguishing between the polar covalent bond (case of BrF) and the ionic bond (case of LiF) scenario. Only in the latter case the "local sphericity" relationship is obeyed along the internuclear line even beyond the penultimate shell-valence shell boundary up to the valence attractor.

As further quantities to characterize the ELI-D topology, the three constituent terms of relative ELI-D curvature $\tilde{V}_D''/\tilde{V}_D$, ρ''/ρ, and $2(\ln \rho)'(\ln \tilde{V}_D)'$, are added to yield the respective Laplacian quantity $\nabla^2\tilde{V}_D/\tilde{V}_D$, $\nabla^2\rho/\rho$ and $2\nabla \ln \rho \cdot \nabla \ln \tilde{V}_D$. The sum of them yields the relative Laplacian of ELI-D $\nabla^2 Y_D^\sigma/Y_D^\sigma$. It represents a different access to the analysis of ELI-D topology. While for the signature of an ELI-D critical point each of the different terms competes only in one direction, the relative ELI-D Laplacian is dominated by the overall large contributions in any of the three directions. For this reason the sign of the ELI-D Laplacian is inherently given for the attractor and the repellor, being negative and positive, respectively, but not for the saddle points. For these it can be negative like for the attractor or positive like for the repellor. The mathematical interpretation of a negative Laplacian of a scalar quantity is its tendency to locally concentrate at that point.

In the present context the sign of the ELI-D Laplacian has proven valuable. One advantage is its robustness with respect to approximate wave functions. This is caused by the dominance of the globally large terms of all directions. Thus, for F_2, where HF and semilocal DFT give different topologies, the Laplacian gives the same result for both methods. In detail, it allows us to characterize ELI-D saddle points with negative Laplacian as connected to ELI-D attractors (having always negative ELI-D Laplacian), and with positive Laplacian as disconnected from them. This makes it possible to clearly distinguish on a topological basis the inter-closed-shell interaction of the Ne_2 diatomic unit not only from standard shared interactions but also from the shared polar interaction like for F_2.

Furthermore, the evolution of the ELI-D Laplacian terms from single to triple bonds between main group elements provides a characteristic picture of multiple bonding scenario. Although for the single bond scenario the $\nabla^2\rho/\rho$ and the $\nabla^2\tilde{V}_D/\tilde{V}_D$ term are of similar importance, the triple bond ELI-D Laplacian is dominated by the negative contributions from the $\nabla^2\rho/\rho$ term with the $\nabla^2\tilde{V}_D/\tilde{V}_D$ contributions being small and eventually even positive at the ELI-D attractor.

It has been suggested on the basis of an empirically found homeomorphism between the Laplacian of the density and the Laplacian of the conditional same-spin pair density that the former "condenses the essential pairing information determined by the conditional pair density in six-dimensional space" into its topology in three-dimensional position space.[13] On the other hand, ELI-D itself represents a measure for the local pairing of same-spin electrons.[4] Local maxima of ELI-D signify positions with locally maximal pairing avoidance of same spin electrons. The electron pairing information contained in ELI-D is formally brought forth through the multiplication of the electron density with the pair-volume function. The Laplacian of ELI-D does not contain more electron pairing information than ELI-D does, it only displays the pairing information in a locally averaged way: a negative ELI-D Laplacian means that there is locally stronger pairing avoidance than within the close neighborhood on average. It is now interesting to note that the Laplacian of the density occurs only within one term, either $\nabla^2\rho\cdot\tilde{V}_D$ or $\nabla^2\rho/\rho$, of the Laplacian or relative Laplacian, respectively, of ELI-D. It can be seen from the examples analyzed above that the sign of the contributions of the $\nabla^2\rho/\rho$ term often equals the sign of ∇^2Y_D/Y_D, and especially in the proximity of an ELI-D attractor in the valence region, $\nabla^2\rho/\rho$ often displays negative values. But there are also cases (e.g., the F_2 molecule), where the pair-volume function containing terms dominate in the bonding region, and the sign or the topology of $\nabla^2\rho$ or $\nabla^2\rho/\rho$ does not predetermine the sign of ∇^2Y_D/Y_D. In a related context the incomplete homeomorphism between the topologies of the Becke ELF[22] and $-\nabla^2\rho$ for a number of molecules has been reported by Bader et al.[20] Considering the Becke ELF kernel in a certain sense as an approximation to ELI-D, the present investigation contains also a refined analysis of the relation between the local electron pairing extractable from $-\nabla^2\rho$ and from ELF in the sense of ELI-D.

9. Conclusion

For a number of molecules, which exemplarily represent different chemical bonding scenarios, the topology of the ELI-D scalar field has been related to the topologies of its constituent functions, the electron density and the pair-volume function. Although they represent physically different quantities, their topologies are shown to be related in a typical way for the examples analyzed. Typically, there are correspondences between the bond critical, ring critical and cage critical points occurring in the electron density and those critical points of the pair-volume function. Even if they do not coincide, the curvatures of a corresponding pair of critical points display the opposite sign. The location of ELI-D critical points and their signatures are shown to be related to the topologies of the electron density and the pair-volume function in a way, which depends on the type of chemical interaction. The introduction of the relative ELI-D Laplacian and the analysis of its constituent terms has been shown to yield useful information on the chemical bonding scenario. This opens a novel way to distinguish different chemical bonding types on a quantum mechanical basis in the framework of ELI-D. Unsurprisingly, the observed differences occur on a continuous scale. Nature does not know black and white, nor gray: it is colored. The occurrence of the electron density in the formula of ELI-D and of the Laplacian of the density in one term of the ELI-D Laplacian establishes a physical link between properties derived from the pair density like electron localizability and electron pairing and the 1-particle properties connected with the electron density.

Acknowledgment. Funding by the Deutsche Forschungsgemeinschaft (priority program SPP 1178) is acknowledged.

References and Notes

(1) Bader, R. F. W.; Beddall, P. M. *J. Chem. Phys.* **1972**, *56*, 3320–3329.
(2) Bader, R. F. W. *Atoms in Molecules-A Quantum Theory*; Clarendon Press, Oxford, U.K., 1995.
(3) Bader, R. F. W.; Heard, G. L. *J. Chem. Phys.* **1999**, *111*, 8789–8798.
(4) Kohout, M. *Int. J. Quantum Chem.* **2004**, *97*, 651–658.
(5) Kohout, M. *Faraday Discuss.* **2007**, *135*, 43–54.
(6) Wagner, F. R.; Bezugly, V.; Kohout, M.; Grin, Yu. *Chem. Eur. J.* **2007**, *13*, 5724–5741.
(7) Kohout, M. To be published.
(8) Becke, A. D. *Int. J. Quantum Chem.* **1985**, *27*, 585–594.
(9) Wang, W.-P.; Parr, R. G. *Phys. Rev. A* **1977**, *16*, 891–902.
(10) Pendàs, A. M.; Blanco, M. A.; Costales, A.; Sanchez, P. M.; Luana, V. *Phys. Rev. Lett.* **1999**, *83*, 1930–1933.
(11) Collard, K.; Hall, G. G. *Int. J. Quantum Chem.* **1977**, *12*, 623–637.
(12) Bader, R. F. W.; MacDougall, P. J.; Lau, C. D. H. *J. Am. Chem. Soc.* **1984**, *106*, 1594–1605.
(13) Bader, R. F. W.; Hernandez-Trujillo, J.; Cortez-Guzman, F. *J. Comput. Chem.* **2007**, *28*, 4–14.
(14) (a) te Velde, G.; Bickelhaupt, F. M.; van Gisbergen, S. J. A.; Fonseca Guerra, C.; Baerends, E. J.; Snijders, J. G.; Ziegler, T. *J. Comput. Chem.* **2001**, *22*, 931–967. (b) Fonseca Guerra, C.; Snijders, J. G.; te Velde, G.; Baerends, E. J. *Theor. Chem. Acc.* **1998**, *99*, 391–403. (c) ADF2006.01, SCM, Theoretical Chemistry, Vrije Universiteit, Amsterdam, The Netherlands, http://www.scm.com.
(15) Becke, A. D. *Phys. Rev. A* **1988**, *38*, 3098–3100.
(16) Lee, C.; Yang, W.; Parr, R. G. *Phys. Rev. B* **1988**, *37*, 785–789.
(17) Kohout, M. *Program DGrid, version 4.2*, Dresden, 2007.
(18) Kato, T. *Commun. Pure Appl. Math.* **1957**, *10*, 151–177.
(19) Bader, R. F. W.; Essen, H. *J. Chem. Phys.* **1984**, *80*, 1943–1960.
(20) Bader, R. F. W.; Johnson, S.; Tang, T.-H.; Popelier, P. L. A. *J. Phys. Chem.* **1996**, *100*, 15398–15415.
(21) Bader, R. F. W.; Slee, T. S.; Cremer, D.; Kraka, E. *J. Am. Chem. Soc.* **1983**, *105*, 5061–5068.
(22) Becke, A. D.; Edgecombe, K. D. *J. Chem. Phys.* **1990**, *92*, 5397–5403.

JP8022315